DISCLAIMER

U.S. DEPARTMENT OF ENERGY | Office of NUCLEAR ENERGY | SPENT FUEL & HIGH-LEVEL WASTE DISPOSITION

Uncertainty and Sensitivity Analysis Methods and Applications in the GDSA Framework (FY2025)

Spent Fuel and Waste Science and Technology Campaign

Prepared for
U.S. Department of Energy
Office of Nuclear Energy
By Sandia National Laboratories

Laura P. Swiler[1], Eduardo Basurto[1], Dusty M. Brooks[1], Tara LaForce[1], Rosemary Leone[1], Paul E. Mariner[1], Teresa Portone[1], Caitlin Condon[2], Josh Hargraves[2], Tristan Hay[2]

August 22, 2025

M3SF- 252SN010304072
SAND2025-11744R

[1] Sandia National Laboratories
[2] Pacific Northwest National Laboratory

National Nuclear Security Administration

Sandia National Laboratories

Sandia National Laboratories is a multimission laboratory managed and operated by National Technology & Engineering Solutions of Sandia, LLC., a wholly owned subsidiary of Honeywell International, Inc., for the U.S. Department of Energy's National Nuclear Security Administration under contract DE-NA0003525.

NFCSC DOCUMENT COVER SHEET[1]

Name/Title of Deliverable/Milestone/Revision No.	Uncertainty and Sensitivity Analysis Methods and Applications in the GDSA Framework (FY2025)
Work Package Title and Number	GDSA - Uncertainty and Sensitivity Analysis Methods – SNL SF-25SN01030407
Work Package WBS Number	SF-25SN01030407
Responsible Work Package Manager	Laura P. Swiler (Name/Signature)
Date Submitted	08/22/2025

Quality Rigor Level for Deliverable/Milestone[2]	☐ QRL-1 ☐ Nuclear Data	☐ QRL-2	☒ QRL-3	☐ QRL-4 Lab QA Program[3]

This deliverable was prepared in accordance with Sandia National Laboratories QA program, which meets the requirements of:

☒ DOE Order 414.1 ☐ NQA-1 ☐ Other

This deliverable was subjected to:

☒ Technical Review (TR) ☐ Peer Review (PR)

TR Documentation Provided
☐ Signed TR Report, or
☐ Signed TR Concurrence Sheet, or
☒ Signature of TR Reviewer(s) below

PR Documentation Provided
☐ Signed PR Report, or
☐ Signed PR Concurrence Sheet, or
☐ Signature of PR Reviewers below

Name and Signature of Reviewers

Laura Price

NOTE 1: *This form should be filled out and submitted with the deliverable. Or, if the PICS:NE system permits, completely enter all applicable information in the PICS:NE Deliverable Form. The requirement is to ensure that all applicable information is entered either in the PICS:NE system or by using the NFCSC Document Cover Sheet.*

- *In some cases, there may be a milestone where an item is being fabricated, maintenance is being performed on a facility, or a document is being issued through a formal document control process where it specifically calls out a formal review of the document. In these cases, documentation (e.g., inspection report, maintenance request, work planning package documentation or the documented review of the issued document through the document control process) of the completion of the activity, along with the Document Cover Sheet, is sufficient to demonstrate achieving the milestone.*

NOTE 2: *If QRL 1, 2, or 3 is not assigned, then the QRL 4 box must be checked, and the work is understood to be performed using laboratory QA requirements. This includes any deliverable developed in conformance with the respective National Laboratory / Participant, DOE or NNSA-approved QA Program.*

NOTE 3: *If the lab has an NQA-1 program and the work to be conducted requires an NQA-1 program, then the QRL-1 box must be checked in the work Package and on the Appendix E cover sheet and the work must be performed in accordance with the Lab's NQA-1 program. The QRL-4 box should not be checked.*

EXECUTIVE SUMMARY

1 SUMMARY INTRODUCTION

The Spent Fuel and Waste Science and Technology Campaign (SFWST) of the U.S. Department of Energy (DOE) Office of Nuclear Energy (NE) is conducting research and development on geologic disposal of spent nuclear fuel (SNF) and high-level nuclear waste (HLW). Two priorities for SFWST are design concept development and disposal system modeling. These priorities are directly addressed in the Geologic Disposal Safety Assessment (GDSA) control account, which is charged with developing a geologic repository system modeling and analysis capability, and the associated software, GDSA Framework, for evaluating disposal system performance for nuclear waste in geologic media.

This report describes specific activities in the Fiscal Year (FY) 2025 associated with the GDSA Uncertainty and Sensitivity Analysis Methods work package. This report fulfills the GDSA Uncertainty and Sensitivity Analysis Methods work package (SF-25SN01030407) level 3 milestone, Uncertainty and Sensitivity Analysis Methods and Applications in GDSA Framework (FY2025) (M3SF-25SN010304072). This work was closely coordinated with the other Sandia National Laboratory GDSA work packages: the GDSA Framework Development work package (SF-25SN01030408), the GDSA Repository Systems Analysis work package (SF-25SN01030409), and the GDSA PFLOTRAN Development work package (SF-25SN01030410). This report builds on developments reported in previous GDSA Framework milestones, particularly M3SF-24SN010304072.

1.1 HIGH-LEVEL PURPOSE OF THIS WORK:

Performance assessment (PA) for underground geologic disposal of nuclear waste is an iterative process for determining the safety relevant set of features, events, and processes (FEPs) to include in a PA model. Probabilistic PA model simulations are performed to estimate the full range of behavior of the system including the pertinent variability and uncertainty in the system. Results are evaluated against system performance metrics (e.g., for evaluating key sensitivities needing further constraints or for assessing performance against regulatory requirements). A fundamental use of uncertainty and sensitivity analyses is the determination of uncertain parameters that are most impactful to changes in performance. This determination is useful for decision makers as they develop future development priorities for a given repository setting. This use of SA/UQ will be fundamentally important to the U.S. program going forward.

1.2 FY25 ACCOMPLISHMENTS

1) Sensitivity analysis for a near-field shale case. This was a simplified case, a “quarter waste package” case, that was highly refined around the waste package to better understand maximum temperatures and pressures at various points in and near the repository. Ten uncertain input parameters were varied and 200 PFLOTRAN runs launched for the SA results.
2) Sensitivity analysis for the biosphere model. The GDSA UQ/SA team worked closely with the GDSA Biosphere model development team at PNNL to demonstrate an integrated workflow where Dakota generated sample parameter values both for the PFLOTRAN model and for the Biosphere model and ran them in a coupled, sequential fashion as part of a sensitivity analysis.
3) International activities. We continue to engage in and support international activities. This year, we are supported the UQ/SA activities for the crystalline task of the 2024-2027 phase of DECOVALEX. We completed Volume 2 with the Joint Sensitivity Analysis Working Group (JOSA) summarizing the result of various SA studies on the case studies provided by the participating organizations and are continuing with new case studies and methods in Volume 3.

4) Additional activities. We support training sessions and seminars as requested, including on the Next Generation Workflow which integrates Dakota, PFLOTRAN, the Biosphere model, and potentially other codes and analysis tools. We also continue investigation into state-of-the-art SA methods.

ACKNOWLEDGMENTS

This report has benefited from the insights and assistance of many. The authors thankfully acknowledge Heeho Park and Rosie Leone for their help with PFLOTRAN. The authors acknowledge the GDSA Biosphere Model development team, including Caitlin Condon, Josh Hargraves, and Tristan Hay, all at PNNL. The collaboration with the Biosphere team has been essential for integrating that model into the Dakota/PFLOTRAN workflow to perform sensitivity studies.

The authors appreciate and thank the technical reviewers for comments and suggestions that improved the quality of the manuscript. Finally, the authors give a special thanks to Daniel Fagnant of the Department of Energy's Spent Fuel and Waste Science and Technology Campaign for his on-going support and guidance.

CONTENTS

LIST OF FIGURES

LIST OF TABLES

ACRONYMS

CDF	Cumulative Distribution Function
DOE	U.S. Department of Energy
DFN	Discrete Fracture Network
DRZ	Disturbed Rock Zone
GDSA	Geologic Disposal Safety Assessment
GUI	Graphical User Interface
HLW	High-level waste
HPC	High Performance Computing systems
JOSA	Joint Sensitivity Analysis working group
LHS	Latin Hypercube Sampling
Ma	mega annum (one million years)
NGW	Next Generation Workflow
PA	Performance Assessment
PCE	Polynomial Chaos Expansion
PNNL	Pacific Northwest National Laboratory
QoI	Quantity of Interest
R&D	Research and Development
SA	Sensitivity Analysis
SFWST	Spent Fuel and Waste Science and Technology Campaign
SNL	Sandia National Laboratories
UQ	Uncertainty Quantification
WP	Waste Package

SPENT FUEL AND WASTE SCIENCE AND TECHNOLOGY CAMPAIGN, GEOLOGIC DISPOSAL SAFETY ASSESSMENT, SENSITIVITY ANALYSIS AND UNCERTAINTY QUANTIFICATION

1 INTRODUCTION

This report presents high level objectives and strategy for development of uncertainty and sensitivity analysis tools in Geologic Disposal Safety Assessment (GDSA) Framework, a software toolkit for probabilistic post-closure performance assessment (PA) of systems for deep geologic disposal of nuclear waste. GDSA Framework is supported by the Spent Fuel and Waste Science and Technology Campaign of the U.S. Department of Energy (DOE), Office of Nuclear Energy (NE).

This report fulfills the GDSA Uncertainty and Sensitivity Analysis Methods work package (SF-25SN01030407) level 3 milestone, Uncertainty and Sensitivity Analysis Methods and Applications in GDSA Framework (FY2025) (M3SF-25SN010304072). It presents high level objectives and strategy for development and demonstration of uncertainty quantification (UQ) and sensitivity analysis (SA) tools in GDSA Framework in fiscal year 2025 (FY25).

This work was closely coordinated with the other Sandia National Laboratory GDSA work packages: the GDSA Framework Development work package (SF-25SN01030408), the GDSA Repository Systems Analysis work package (SF-25SN01030409), and the GDSA PFLOTRAN Development work package (SF-25SN01030410). This report builds on developments reported in previous GDSA Framework milestones, including M3SF-24SN010304072 (Swiler L. P., et al., 2024), M3SF-23SN010304072 (Swiler, et al., 2023), M3SF-22SN01030482 (Swiler L. P. , et al., 2022), M3SF-21SN010304042 (Swiler L. P., et al., 2021), M3SF-20SN010304032 (Swiler L. P., et al., 2020), and M3SF-19SN010304032 (Swiler, et al., 2019).

Geologic repository performance assessment in the U.S. involves a code base that includes coupled, multiphysics modeling at high resolution. Due to the high computational cost of these models which require high performance computing systems (HPC) to run, relatively few simulation samples are available for analysis. This highlights the need to consider surrogate models to sample and explore the input parameter space more extensively. However, this must be done in a careful way so that surrogate accuracy can be tracked and understood in the context of UQ/SA results. Variance-based sensitivity indices are now a standard practice in the sensitivity analysis community but require many evaluations of the predictive model. Much research has focused on accurately calculating variance-based sensitivity indices while keeping the computational cost reasonable. We note that other sensitivity analysis methods (Swiler, et al., 2019) may be better than variance-based methods at identifying patterns of behavior or trends. Another recent approach is to employ “multifidelity” UQ in which many low-fidelity simulation runs (e.g., coarser mesh, simpler physics) augment a small number of high-fidelity runs (Swiler L. P., et al. 2021; Swiler L. P., et al., 2020). Keeping abreast of improvements to existing UQ/SA methods as well as employing new methods is critical to performing sensitivity and uncertainty analysis of new repository systems which will involve large parameter spaces and computationally expensive simulations. The repository community must maintain awareness of and leadership in UQ/SA methods to best inform our assessment of costly computational models.

1.1 OVERVIEW OF THIS REPORT

This report provides documentation of the UQ/SA work performed in FY 2025. The outline of this report is as follows:

Chapter 2 provides sensitivity analysis results for PFLOTRAN coupled to the GDSA Biosphere Model. The SA demonstrated the Dakota-PFLOTRAN-GDSA Biosphere modeling coupling, where PFLOTRAN

provides radionuclide concentrations that are inputs to the Biosphere model which is then used to calculate dose.

Chapter 3 summarizes a report we produced this year on spatial heterogeneity treatment (e.g. varying discrete fracture networks) in sensitivity analysis for waste repositories.

Chapter 4 presents UQ and SA results for a near-field, quarter waste package shale case. This is a case study we developed to better understand maximum temperatures and pressures in and around the repository for our generic shale reference case. In this single waste package case, we examined temperature, pressure, and liquid saturation at many observation points in the waste package, the buffer, the disturbed rock zone, and the near-field shale region.

Chapter 5 covers international activities including participation of the GDSA UQ/SA team in the international JOSA working group and in the next 2024-2027 DECOVALEX phase.

Chapter 6 presents a summary.

1.2 GDSA FRAMEWORK

GDSA Framework (Figure 1-1) capabilities include multi-physics simulation of coupled processes affecting deep geologic repository performance, uncertainty and sensitivity analysis, pre- and post-processing, and visualization. For a given performance assessment, these tools will be linked to a version-controlled parameter database and an automated run-control system. The overall objectives of *GDSA Framework* development are to:

- create a framework that is flexible enough to take advantage of future advances in hardware, software, simulation, and analysis methods;
- leverage existing high-performance computing capabilities (e.g., meshing, simulation, analysis, and visualization);
- enable increasingly coupled, mechanistic multi-physics modeling;
- provide analysis methods for prioritization of SFWST Disposal Research activities;
- provide transparent implementation of simulation and analysis methods;
- develop and distribute in an open-source environment so that software is freely available to stakeholders (e.g. see GDSA reports from 2015 through 2024: (Mariner, Gardner, Hammond, Sevougian, & Stein, 2015), (Mariner, et al.,, 2016), (Mariner, Stein, Frederick, Sevougian, & Hammond,, 2017), (Swiler L. P., et al., 2021), (Swiler L. P., et al., 2024).

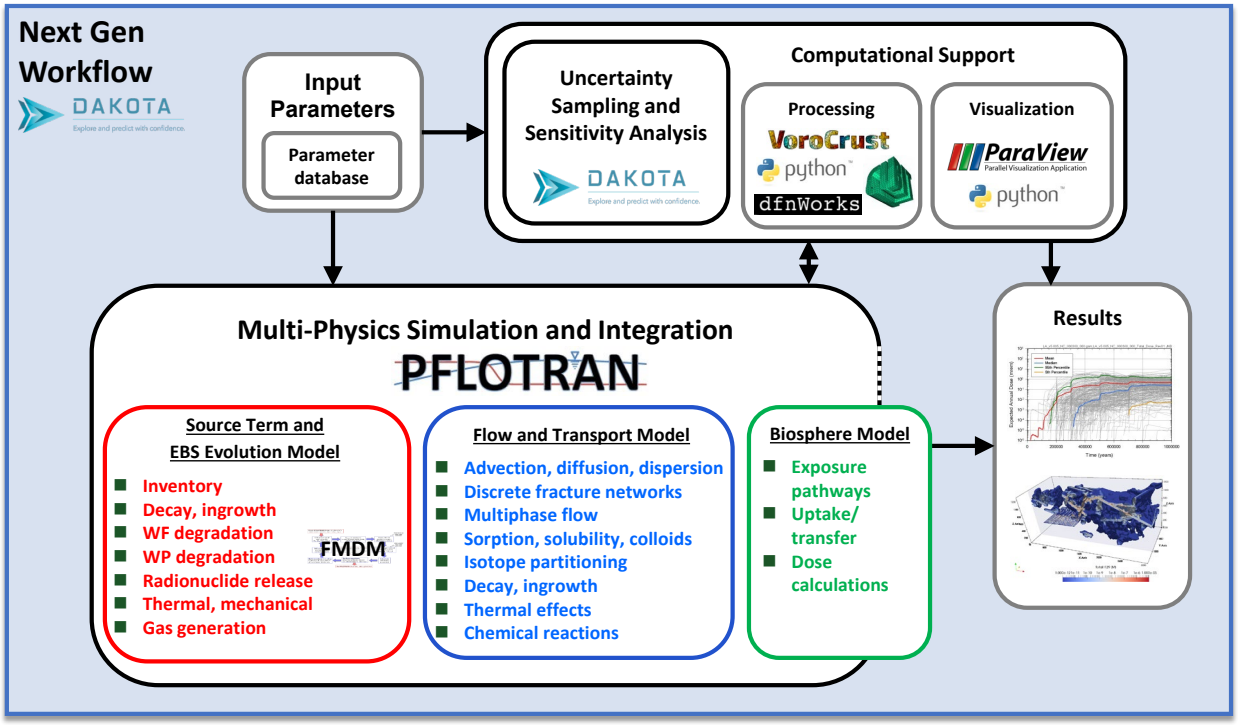

Figure 1-1. The GDSA Framework

One objective of developing the UQ/SA capability in GDSA Framework is to standardize sampling-based methods of uncertainty propagation, sensitivity analysis, and uncertainty quantification typically used within U.S. nuclear waste disposal programs (e.g., (U.S. DOE, 2008), (U.S. DOE, 2014), RESS2000 (Helton & Marietta (Editors), Special Issue: The 1996 Performance Assessment for the Waste Isolation Pilot Plant, 2000), RESS2014 (Helton, Hansen, & Swift (Editors), Special Issue: Performance Assessment for the Proposed High-Level Radioactive Waste Repository at Yucca Mountain, Nevada, 2014)). Another objective is to enable future adoption of new methods consistent with the current standard of practice in the UQ/SA community which are appropriate for high-dimensional, highly coupled, nonlinear problems resulting from the implementation of mechanistic multi-physics simulations. Having a consistent, common framework which enables a user to perform a range of sensitivity analysis and UQ approaches for a particular problem or set of simulations allows for reproducibility, comparative analyses, use of verified algorithms, and documentation of best practices. These are important goals for performance assessments.

The following sections highlight the key components of *GDSA Framework*. More information about each can be found by following the links at https://pa.sandia.gov.

1.2.1 PFLOTRAN

PFLOTRAN is an open source, state-of-the-art, massively parallel subsurface flow and reactive transport simulator (Lichtner & Hammond, 2012; Hammond, Lichtner, Mills, & Lu,, 2008; Hammond, Lichtner, & Mills, 2014) written in object-oriented Fortran. PFLOTRAN models subsurface flow using a porous medium continuum approach, which includes capabilities for multicomponent systems, multiphase flow and transport, heat conduction and convection, biogeochemical reactions, geomechanics, and radionuclide decay and ingrowth. The software is developed under a GNU Lesser General Public License, which allows third parties to interface PFLOTRAN with proprietary software. The availability and continuing development of PFLOTRAN for GDSA are due to an ongoing collaborative effort of several DOE laboratories led by Sandia. PFLOTRAN development for *GDSA*

Framework is described by Mariner et al. (Mariner, et al., 2018; Mariner, Stein, Frederick, Sevougian, & Hammond, 2017; Mariner, et al., 2016) and Sevougian et al. 2018. PFLOTRAN installation instructions and documentation are available at https://www.pflotran.org/.

1.2.2 DAKOTA

Dakota is an open-source toolkit of algorithms that contains both state-of-the-art research and robust, usable software for optimization and UQ. It is available at: https://dakota.sandia.gov (Adams, et al., 2022). The Dakota software has parametric analysis methods that enable design exploration, model calibration, optimization, uncertainty quantification, and sensitivity analysis with computational models. Dakota is a C++ code which has been under development at Sandia since 1994. It has been primarily sponsored by DOE's Advanced Simulation and Computing (ASC) program. Dakota supports computationally expensive simulations which require high performance computing and parallel execution. Thus, a focus of the algorithm development in Dakota has been on methods that are as efficient as possible and minimize the number of runs required of a high-fidelity simulation model.

Dakota contains the UQ/SA methods typically used in the U.S. repository program. Dakota implements Latin Hypercube Sampling (LHS) with correlation control on input parameters. It calculates moments on responses of interest as well as correlation matrices (simple, partial, and rank correlations) between inputs and outputs. Dakota allows nested studies to perform an "outer loop" epistemic sampling and an "inner loop" aleatory sampling to generate ensembles of distributions. Dakota includes additional capabilities, such as the use of surrogate models, adaptive sampling approaches, and multifidelity UQ methods. Dakota returns tables of input and output amenable to further processing and visualization with additional tools developed within *GDSA Framework* or by an individual user.

A graphical depiction of Dakota interfacing with a computational model such as a repository simulation in PFLOTRAN is shown in Figure 1-2. Based on the type of study being performed (optimization, uncertainty quantification, etc.), Dakota chooses the next set of parameters at which to evaluate the simulator and runs the simulator, which returns the performance metrics of interest back to Dakota. Dakota then generates the next set of parameters according to the algorithm being used for the study and keeps iterating until the specified number of samples is reached.

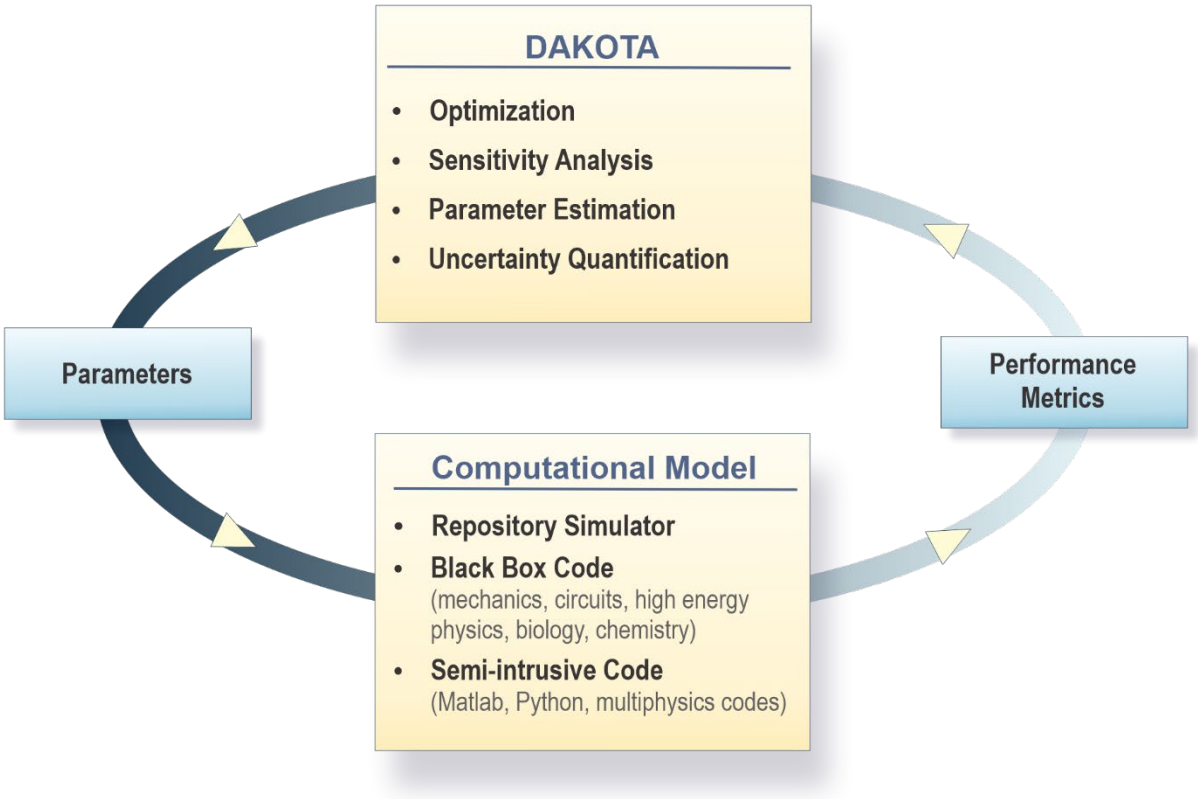

Figure 1-2. Dakota interfacing to a computational model such as a repository simulator

The UQ/SA methods implemented in Dakota have evolved as the standard of practice evolves. Over the past ten years, the Dakota team has invested in methods which calculate the Sobol' variance-based sensitivity indices in an efficient manner. These indices estimate the proportion of variance in a quantity of interest that can be attributed to variance in each uncertain input parameter. Currently, a Dakota user can calculate these by extensive sampling of the simulation code, by using surrogate methods such as regression or Gaussian process models, by the use of polynomial chaos expansions, and by using multifidelity methods. Dakota is an actively maintained and developed code with formal releases issued twice per year. Dakota uses formal software quality development processes including advanced version control, unit and regression testing, agile programming practices, and software quality assessment.

1.2.3 AUTOMATED ANALYSIS WORKFLOW DEVELOPMENT FOR GDSA

Uncertainty Quantification analysis workflows are not trivial to define and get running, even when using tools such as Dakota to generate nested studies involving sampling loops over both aleatory and epistemic samples. The analyst has to spend a significant amount of time writing scripts to interface the sample values to PFLOTRAN, extract the results, and put the entire workflow on a high-performance computing platform. Further, as the number of quantities of interest increases and many vectors of results are generated for each simulation, plotting and aggregating the results in a variety of ways (e.g., averaging over epistemic or aleatory slices as a function of time) becomes very involved. To address this, a set of workflows which couple Dakota, PFLOTRAN, and NGW (the Next-Generation Workflow software) were developed. The workflows present the user with a unified graphical user interface (GUI) where the actual workflow can be dictated and automated in an easy-to-use graphical

format. This workflow also allows greater reproducibility and traceability of the actual files and scripts used for a particular study.

The *Crystalline Reference Case UA Nested Workflow* was developed in FY20, FY21, and FY22 (Swiler L. , et al., 2020; Swiler L. , et al., 2021; Swiler L. , et al., 2022). The portability and automation provided by the workflow significantly speed up the overall analysis. This year, we used NGW to develop the workflow to generate the shale case results presented in Chapter 4.

Also, additional training materials and modifications to the workflow were made this year to increase the robustness of production UQ analyses that run over the span of several weeks. These runs are typically orchestrated by a local compute resource that submits large-scale simulation runs to remote HPC resources with job scheduling. Source files can be distributed across several shared filesystems. The distributed nature of computation and source files means there are many points of failure in these production runs: if any one of the filesystems or compute resources goes down, e.g., for maintenance, the entire workflow fails. To mitigate this issue as much as possible, all source files are copied to the scratch directory of the HPC resource where large-scale simulations will be completed prior to launching the UQ analysis. By centralizing source files and computation to a single resource, the workflow has fewer points of failure, making it more robust over the days-to-weeks timespans it must run.

1.2.4 GDSA SOFTWARE STRATEGY

Developing GDSA Framework in an open-source environment promotes collaboration with regulators, stakeholders, and the scientific community, facilitates development of the software, and enhances communication in a regulatory environment. *GDSA Framework* is being developed currently for generic disposal concepts so that it is poised to be applied efficiently in future programs to specific disposal concepts that may be evaluated for comparison to regulatory safety criteria.

2 SENSITIVITY ANALYSIS: BIOSPHERE MODEL

This chapter summarizes the result of a collaboration between the GDSA Biosphere modeling group at Pacific Northwest National Laboratory (PNNL) and the UQ/SA team at Sandia National Laboratories (SNL). This collaboration started in FY2024, when Dakota was integrated with the biosphere model to "drive" various runs of the biosphere model with different parameter values (see Chapter 2 of (Swiler L. P., et al., 2024). The PNNL and SNL teams performed sensitivity analyses to understand which parameters were important for various scenarios. This year, the computational workflow has been extended to include PFLOTRAN "in the loop." We developed a workflow in which Dakota samples uncertain parameters both for PFLOTRAN and the biosphere model. Further, each run of PFLOTRAN is followed by a biosphere simulation to generate dose calculations.

Recall that the GDSA framework can incorporate Dakota as a "wrapper" around PFLOTRAN or another simulation code to generate ensembles of simulations based on Monte Carlo sampling as shown in Figure 2-1.

Figure 2-1 Workflow with Dakota driving ensembles of PFLOTRAN simulations

This year, we have extended this workflow to include the biosphere model as shown in

Figure 2-2:

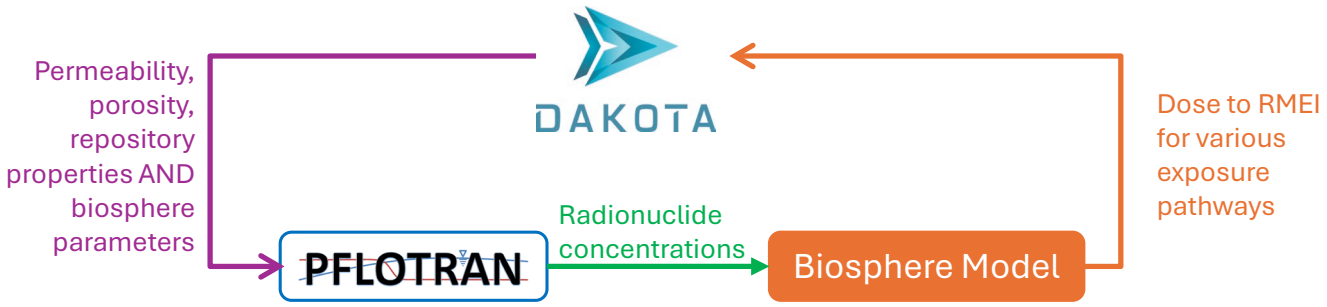

Figure 2-2 Workflow with Dakota driving coupled ensembles of PFLOTRAN simulations followed by Biosphere model simulations

As seen in Figure 2-2, the workflow first involves running PFLOTRAN to generate radionuclide concentrations at various observation points. These are then input to the biosphere model along with

biosphere parameters defining exposure pathways (e.g. drinking water, flora or fauna consumption) to calculate dose to a reasonably maximally exposed individual (RMEI).

This chapter provides a summary of the biosphere model, then describes the case study demonstrating Dakota driving the coupled (PFLOTRAN-Biosphere) model calculations. Note that this case study is not realistic: it is meant to establish and prove out the capability to use the GDSA framework (specifically Dakota, PFLOTRAN, and the Biosphere model) to generate coupled simulation ensemble results.

2.1 BIOSPHERE MODEL DESCRIPTION

The GDSA biosphere model is developed at PNNL. A detailed design document for the GDSA biosphere model is available (Ghosh, et al., 2023). We summarize key concepts of the biosphere model that are relevant to the sensitivity analysis performed herein. The biosphere model is a flexible, open-source code designed for compatibility with PFLOTRAN. The GDSA biosphere model will be capable of modeling a variety of climate scenarios and user exposure pathways, with the aim of supporting performance assessment analyses for repositories. The biosphere model calculates annual dose of dissolved radionuclides to a hypothetical RMEI living near the repository with repository-contaminated groundwater as the sole source of water. The full biosphere model will include all the pathways of exposure for the RMEI shown in Figure 2-3.

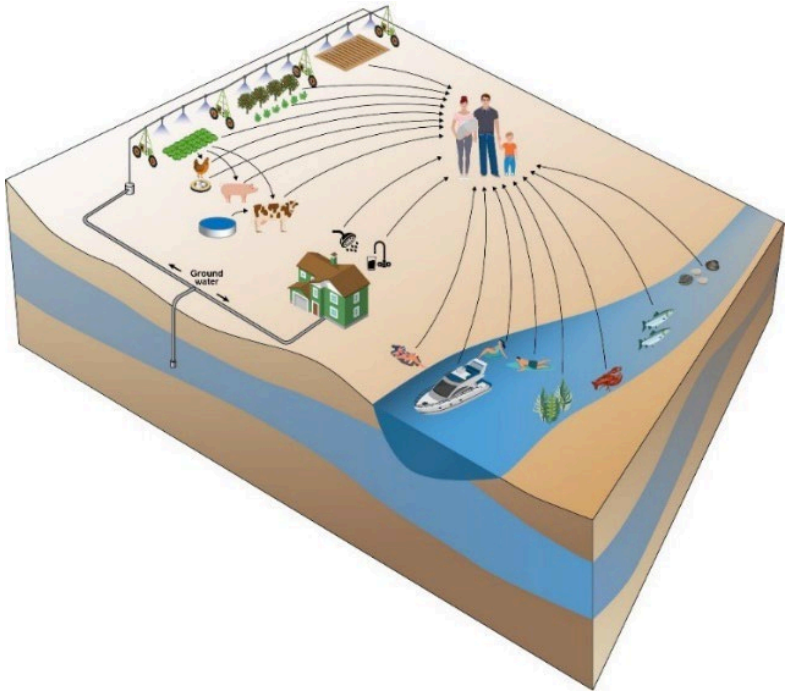

Figure 2-3 Biosphere model exposure pathways to reasonably maximally exposed individuals, which are indicated by the terminus of the arrows in the illustration.

Properties that may impact the estimated dose to a RMEI include, but are not limited to: the radionuclides to which the RMEI is exposed, the degree to which radionuclide concentrations are diluted in surface water (fed from ground water), called the “dilution factor”; soil properties such as soil thickness, weathering rate (how rapidly soil is depleted), infiltration rate, bulk density, and moisture content; plant crop yield and holdup time (time between harvest and consumption); transfer factors between environmental media in exposure pathways; and consumption rates of different environmental media, such as leafy vegetables.

The computational workflow coupling PFLOTRAN and the Biosphere model within an uncertainty quantification study is illustrated in Figure 2-4. Dakota generates uncertain input samples for the PFLOTRAN and Biosphere simulations. In the example presented in this chapter, we use the sample framework of the generic crystalline reference case as described in (Swiler L., et al., 2022), where the sampling involves both spatial heterogeneity (e.g. samples of discrete fracture networks) as well as epistemic parameters such as porosity and permeability of the buffer, fractional dissolution rate of the spent nuclear fuel, waste package corrosion rate, etc. After the PFLOTRAN simulation is completed, the PFLOTRAN-computed groundwater radionuclide concentrations are postprocessed to be used as input to the biosphere model. The radionuclides from the groundwater are introduced to the biosphere environmental media through one or more of the exposure pathways shown in the biosphere model exposure pathway matrix in Figure 2-5. Libraries of radionuclide-specific transfer factors are used to model equilibrium transfer between media components such as groundwater or surface water to soil to plant crops. The biosphere model also tracks radionuclide decay and progeny ingrowth. Total effective dose (TED) is computed as the sum of annual doses over a specified time range. In this work, TED was computed over 70 years, a typical human lifespan, using concentrations from the last 70 years of the PFLOTRAN simulation.

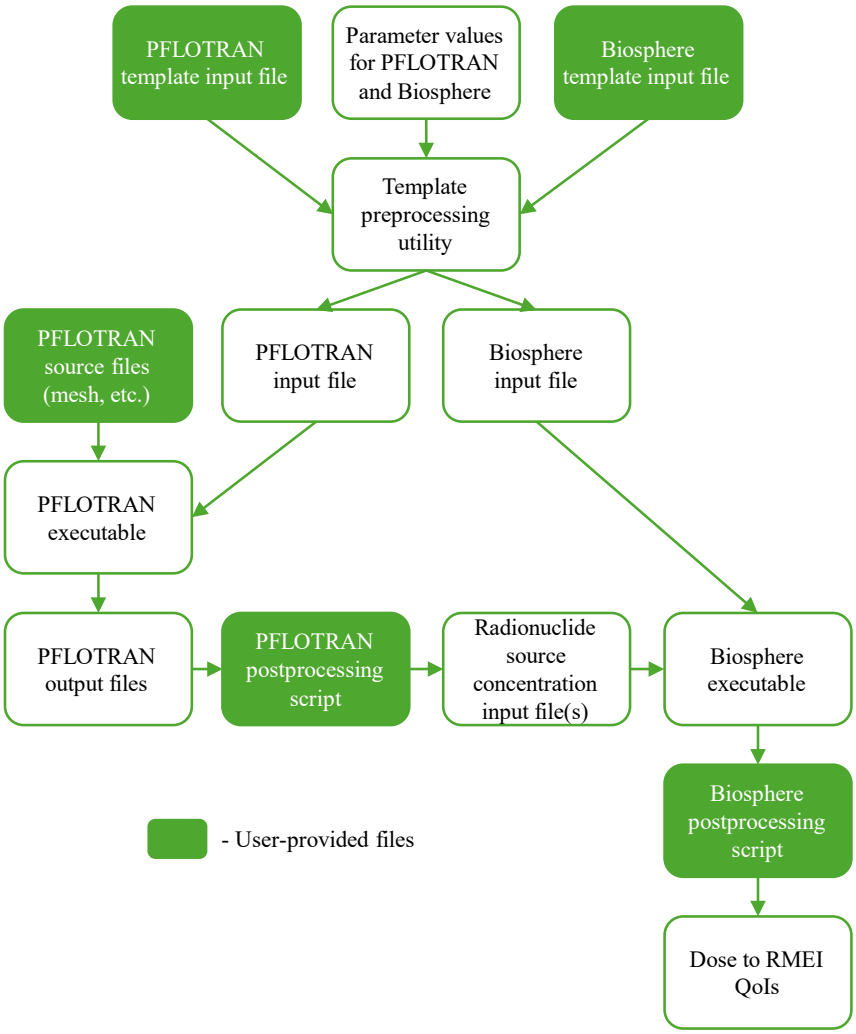

Figure 2-4 Building Blocks for the Dakota-PFLOTRAN-Biosphere model workflow.

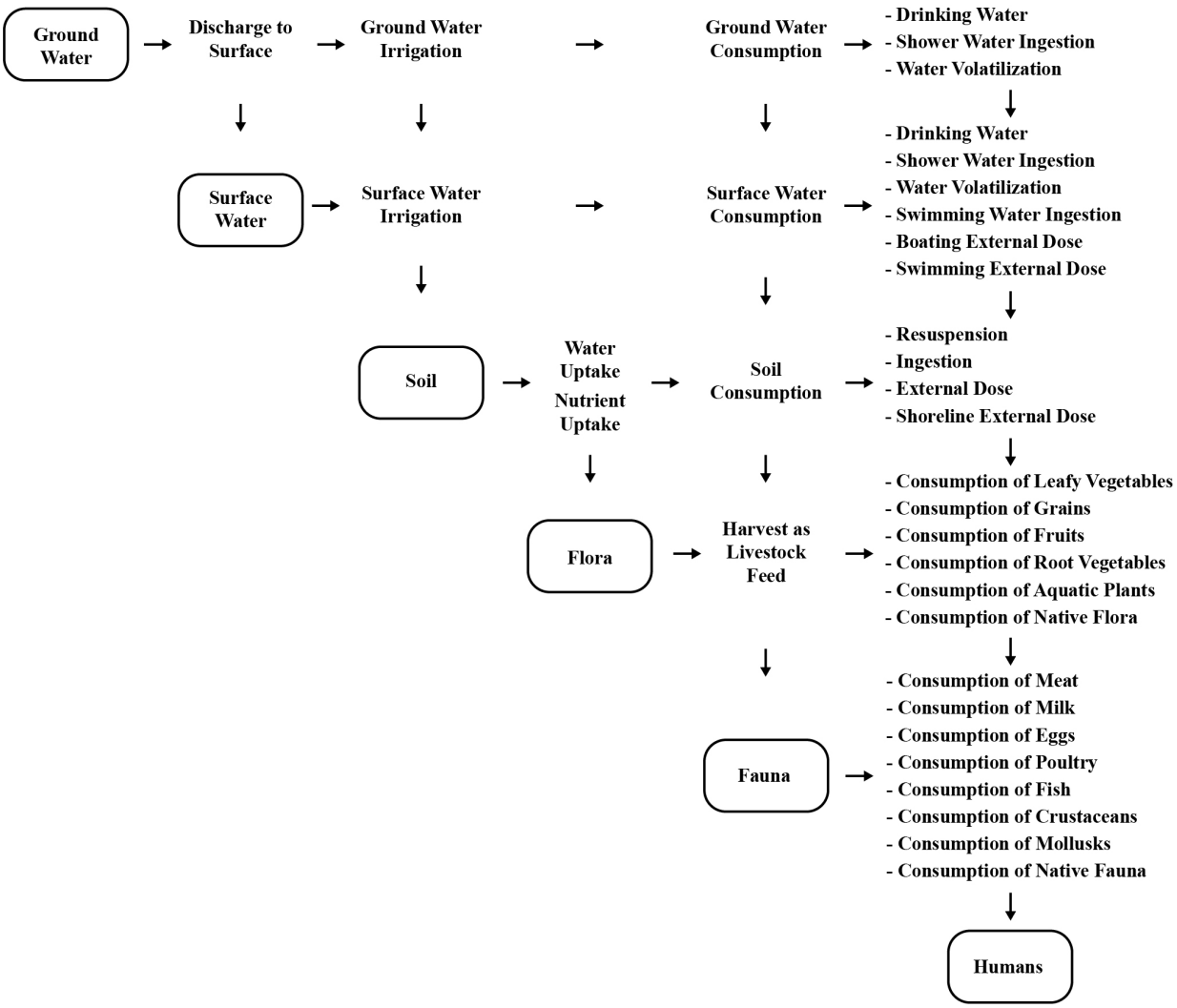

Figure 2-5 Biosphere model exposure pathway matrix. Note that the entries in the far-right column to not feed into each other consecutively but all go directly to the "Humans" category.

2.2 UNCERTAINTY CHARACTERIZATION

In the FY2024 uncertainty analysis for the biosphere model, we included over 40 uncertain parameters and examined sensitivity of RMEI dose to these parameters for three radionuclides, ^{125}I, ^{137}Cs, and ^{226}Ra. This year, we simplified the uncertainty treatment in the biosphere model to focus on the dominant uncertain parameters for ^{129}I. These five important parameters were selected based on running all parameters on an ^{129}I case with a coupled PFLOTRAN/Biosphere/DAKOTA run and were identified as being most impactful. We note that these parameters are important for this ^{129}I radionuclide for this particular set of exposure pathways; other radionuclides and variations of exposure pathways may have different dominant uncertainty parameters. The five biosphere model parameters that were varied are shown in Table 2-1 and include the weathering rate constant and four different Translocation Factors expected to have the greatest impact on dose. All of the Translocation factors are unitless; the weather rate is day. The data for the parameter ranges are from reports PNNL-21950 and PNNL-13421.

Table 2-1 Biosphere Model Parameters sampled as part of the UQ workflow

Variable	Suggested Variable Label	Lower Bound	Upper Bound	Reference
Weathering Rate Constant (day)	DAK_WEATHERING_RATE_CONST	10	20	PNNL-21950
Translocation Factor (Leafy Vegetables)	DAK_TF_TFLV	0.004	0.4	PNNL-13421
Translocation Factor (Root Vegetables)	DAK_TF_TFRV	0.004	0.4	PNNL-13421
Translocation Factor (Fruits)	DAK_TF_TFF	0.004	0.4	PNNL-13421
Translocation Factor (Grains)	DAK_TF_TFG	0.004	0.4	PNNL-13421

2.3 SENSITIVITY ANALYSIS RESULTS

As mentioned above, this workflow and the corresponding results presented here are illustrative and meant to demonstrate the coupled PFLOTRAN-Biosphere ensemble generation. They are not representative of a realistic scenario. In this case study, we generated 1000 PFLOTRAN simulations (varying the discrete fracture network and some epistemic parameters relating to the crystalline reference case). Each of the 1000 PFLOTRAN sample realizations was followed by a Biosphere model simulation. We performed the uncertainty analysis two different ways. In the first study, we generated 1000 PFLOTRAN sample runs and ran the Biosphere model for each of the 1000 PFLOTRAN runs, but we did NOT vary any Biosphere model parameters. That is, all the Biosphere model parameters were set to their nominal values: this is the "Nominal biosphere" study. This study demonstrates the distribution of total effective dose (TED) resulting from uncertainties in the PFLOTRAN simulations alone; these uncertainties are propagated through the ^{129}I concentration to the Biosphere model. The second case is very similar: again, we generated 1000 PFLOTRAN runs (we used the same PFLOTRAN runs as in the nominal biosphere study), but each PFLOTRAN run was followed by a Biosphere model run which did incorporate a sample realization of the five biosphere parameters shown in Table 2-1. Note that we assumed no correlations existed between the sampled PFLOTRAN input parameters and the sampled biosphere model parameters.

Figure 2-6 shows two histograms of outputs. Both histograms involve 1000 samples, where 1000 PFLOTRAN simulation realizations are followed by 1000 biosphere model realizations. The nominal biosphere result does not involve sampling over the biosphere model parameters, but the biosphere UQ result does involve sampling over the biosphere model parameters. Figure 2-6 shows that these two histograms are essentially identical. This indicates that the TED uncertainties in these particular studies were dominated by the PFLOTRAN input parameter uncertainties, not uncertainties in the biosphere model parameters. Again, we emphasize that much more work is needed to develop a fully realistic case study: these are only results demonstrating what could be done with such comparative analyses. Our prior analysis of the generic crystalline reference case used in these studies indicated that there were large uncertainties in ^{129}I concentration and much of the uncertainty was due to the spatial heterogeneity introduced by the varying DFNs.

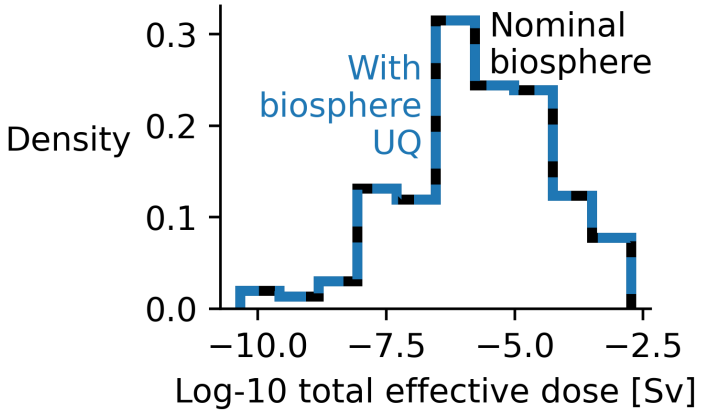

Figure 2-6 Two studies involving coupled PFLOTRAN-Biosphere Model simulations, one with nominal values of biosphere parameters and one varying biosphere model parameters. In both cases, PFLOTRAN simulations involved sample variation.

To further verify differences between the nominal biosphere case and the biosphere model with uncertainty, the two sets of TED results were plotted against each other. This is shown in Figure 2-7. The straight line indicates that the results from both studies (with nominal biosphere model parameters and uncertain biosphere model parameters) align very closely to each other.

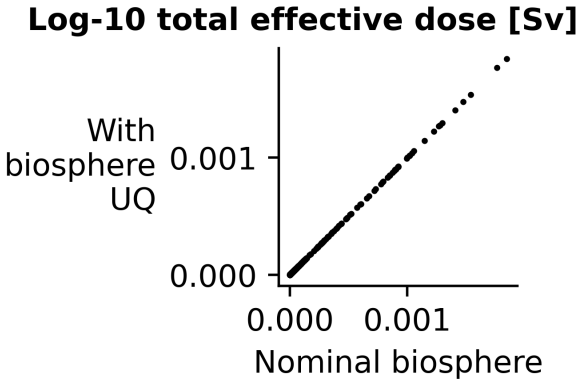

Figure 2-7 Total Effective Dose for the two studies driven by 1000 PFLOTRAN simulations: one with nominal biosphere model parameters, the other with uncertain biosphere model parameters.

To further understand why the results are so strongly dominated by the PFLOTRAN model uncertainty, we fixed the PFLOTRAN sample (e.g. a fixed DFN and one set of epistemic parameter values) and generated 1000 samples of the biosphere model. The results are shown in Figure 2-8, which indicates that the TED variation when sampling only the biosphere model parameters is extremely small, ranging from 7.89E-6 to 7.91E-6. This is not surprising, since the ^{129}I concentrations are very low and the uptake of ^{129}I by the receptor from the environmental media is low. Additionally, as shown in the scatterplots in Figure 2-8, the TED exhibits linear dependence on biosphere parameters, so we do not observe significant influence on dose over the realistic environmental ranges over which the parameters were varied. Finally, we comment on the direction of influence of the translocation factors for leafy vegetables, fruits and root vegetables (positive trend with respect to TED) compared to the trend of the translocation factor for grains (negative trend with respect to TED). We expect the grain component to always have a diminishing effect compared to all other plant forms, especially for a long

lived and non-biologically necessary-equivalent radionuclide such as ^{129}I. The grain component represents the reproductive sink of the plant, with the following properties:

a. Iodine is not essential for seed development.
b. Transport to grain occurs late in plant development.
c. Grain filling competes with other physiological processes.
d. The seed coat can act as a partial barrier to iodine accumulation.
e. This creates inherently lower and more variable TFs for grain compared to vegetative tissues.

For this model case (pathways and radionuclide), the other plant tissues show a positive correlative with TF and TED as there are more opportunities for a "successful" uptake of the radionuclide in these plant tissues.

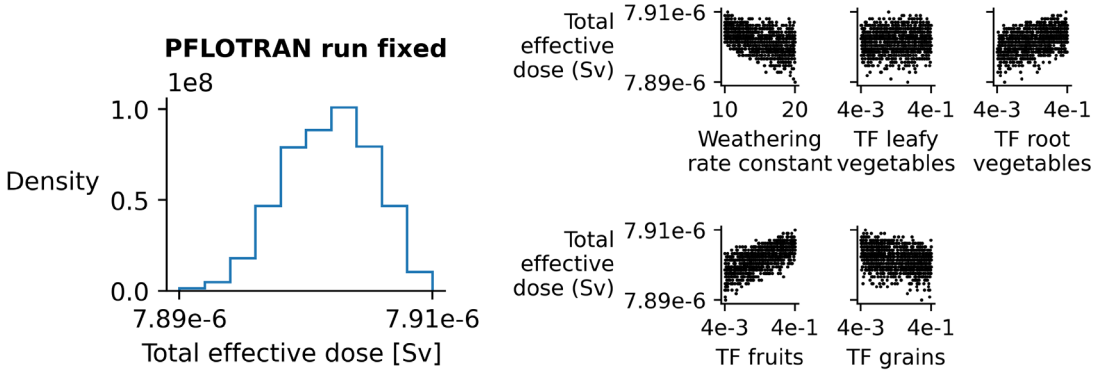

Figure 2-8 Distribution of total effective dose varying only the biosphere model parameters (left) and scatterplots of total effective dose vs. biosphere parameter sample values (right).

The particular uncertain parameters and ranges chosen for the biosphere model do not result in significant differences in the total effective dose. This finding is summarized in Figure 2-9, where the Sobol' main effect index for the uncertainty from the PFLOTRAN radionuclide concentrations is 1 and the main effect indices for the biosphere model parameters are all zero, indicating that all of the uncertainty in TED arises from uncertainty in the PFLOTRAN input variables.

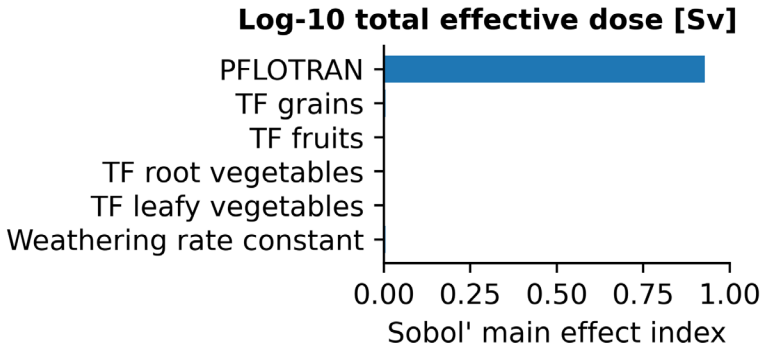

Figure 2-9 Sobol' main effect indices for the TED uncertainty due to the PFLOTRAN output concentrations and the biosphere model parameters.

2.4 CONCLUSIONS AND FUTURE WORK

This work is a demonstration of the integration of the GDSA biosphere model within the GDSA UQ/SA framework. Coupled PFLOTRAN-biosphere simulations were generated with Dakota, and the corresponding results were shown in histograms, scatterplots, and Sobol' indices. Although the dominant uncertainty in these results was from the 1000 PFLOTRAN runs of the generic crystalline reference case, we emphasize that these results are not very realistic: the purpose of this study is to demonstrate the coupled workflows and types of analyses that they can facilitate. We anticipate larger and more realistic case studies in future projects, with the goal of generating an end-to-end uncertainty quantification from repository to dose.

3 TREATMENT OF SPATIAL HETEROGENEITY IN SENSITIVITY ANALYSIS

The last few years, we performed various analyses that highlighted the influence of spatial heterogeneity (as captured by the effects of sampling various discrete fracture networks) in our nested sampling workflows for the generic crystalline reference case. This year, we performed some additional analyses and summarized all of the work in the report:

> "Challenges in quantifying unparameterized spatial uncertainties in deep geologic repositories for nuclear waste." By Teresa Portone, Dusty Brooks, and Laura Swiler. SAND2025-11240. Sandia National Laboratories Technical Report, Albuquerque NM. 2025.

The report describes novel methods to define and assess the quality of proxy variables that summarize the influence of spatial heterogeneity on repository performance quantities of interest (QoIs). These proxy variables are incorporated into surrogate models that can be used for global sensitivity analysis to measure the relative importance of sources of uncertainty to the QoIs. However, in general it is not expected that the proxy variables perfectly capture the influence of spatial heterogeneities, thus impacting surrogate model accuracy. The report thus discusses methods to mitigate a surrogate constructed with proxy variables overfitting to data, as well as methods to assess the accuracy of the surrogate, namely scatterplots and R^2 values between the surrogate and its build points and comparing surrogate-based sensitivities to those computed directly from input-output samples. The report also compares surrogate-based sensitivity results with sensitivity indices calculated by an empirical binning method that does not require a surrogate. Finally, the report demonstrates the importance of comparing sensitivity indices to input-output scatterplots as a further means of assessing the veracity of the results. Understanding and separating the effect of spatial heterogeneity on repository QoIs has proven challenging, especially with the limited number of discrete fracture networks and parameter samples that can be run for realistic problem sizes.

4 SHALE REPOSITORY REFERENCE CASE

In 2024, we performed a detailed sensitivity analysis on a full-scale generic shale reference case (Swiler L. P., et al., 2024) where the model domain was 7215 m (x-axis) × 2055 m (y-axis) × 1200 m (z-axis), representing a shale-hosted repository system in a layered formation. The numerical domain consisted of approximately 10 million unstructured grid cells with approximately half of the grid cells having finer resolution around the repository. This case study had 2050 waste packages (WPs) that each contained 37 assemblies of SNF from a pressurized water reactor (PWR).

As part of the 2024 generic shale reference case study (LaForce T. , et al., 2024), we added observation points close to the centermost waste package to study the maximum pressure and temperature conditions within the repository. The maximum pressure and temperature both peaked at a few thousand years. Overall, the sensitivity analyses generally identified porosity of the host shale rock as the driving uncertainty for maximum temperature and pressure values at an observation point just east of the centermost waste package within the repository (see Section 4.3.4 of the (Swiler L. P., et al., 2024) report). The study indicated a maximum temperature slightly below 110 degrees C and a maximum pressure slightly below 5 MPa. However, the sensitivity analysis results were dependent on the particular uncertain parameters studied and their ranges. This year, we focused on a generic shale case study with refinement in the near-field, to better understand conditions in which the repository might get too hot with pressures that are too high.

The goal of the quarter waste package case is to assess subsurface conditions conducive to disposal of high-heat load waste packages in shale host rock with a focus on pressures and temperatures. While some of the parameters in the sensitivity analysis are the same as the 2024 report, this year's study has a highly refined single waste package model which allows us to investigate the sensitivity to parameters in the engineered barrier system and the host rock near the waste (e.g. porosity, permeability, and thermal conductivity of the buffer, DRZ and shale, DRZ extent, shale thickness above/below the repository).

A short description of the quarter WP case is presented in Section 4.1, and the input parameters and output quantities of interest are described in Section 4.2. Sensitivity analysis results are presented in Section 4.3.

4.1 QUARTER WP SHALE REFERENCE CASE

The chapter covers the sensitivity analyses performed for a shale near-repository model. The full description of the quarter WP shale case is given in (Basurto, et al., 2025). A literature review was performed to inform properties regarding the geometry, waste package, buffer, disturbed rock zone (DRZ), waste package and drift spacing, repository depth, etc. The findings of the literature review are presented in (Basurto, et al., 2025). This study only has one waste package and is simplified in some respects but has a highly refined mesh in and around the waste package. Additional observation points were added near the waste package to study the maximum liquid pressure and temperature conditions. We note that the material layers and thicknesses are the same for the quarter WP shale model as those found in the half-symmetry shale model in (LaForce T. , et al., 2024) but differences in the nearfield measurements of the waste package, buffer, and DRZ exist. Key differences between the half-symmetry shale model and the quarter WP shale model in the nearfield are that:

- The half-symmetry shale model features a square mesh or grid in the nearfield, while the quarter WP shale model has a fine to coarse radial mesh from the WP to the DRZ,
- The minimal radial distances for the half-symmetry shale model are 0.84 m, 2.5 m, and 4.18 m for the WP, buffer, and DRZ, respectively, while the corresponding radial distances for the quarter WP shale model are 0.85 m, 2.55 m, 4.25 m for the WP, buffer, and DRZ as shown in Figure 4-3.

The geometry and mesh generation for the quarter WP shale model were generated using Cubit 17.02, resulting in a total of 38,652 hexagonal cells. The model domain dimensions are 20 m x 15 m x 1200 m, with potential adjustments in the x- and y-directions depending on the initial temperature and pressure simulation results. This quarter WP model incorporates a graded mesh in both the positive and negative z-directions, facilitating a transition from fine to coarse mesh around the drift region. The grid cell sizes vary throughout the model, with the smallest cells located in the WP, buffer, and DRZ regions, gradually increasing in size as the distance from these areas increases. In the upper and lower regions surrounding the drift area, a fixed grid cell size of 5 m is maintained in the x- and z-directions, while the y-direction starts with a thickness of 0.833 m and primarily measures 0.962 m.

The quarter WP shale model has the full vertical extent implemented which includes several material layers in addition to the shale host rock. Figure 4-1 shows a vertical slice through the model domain for the full-scale shale model used in (LaForce T. , et al., 2024). The same vertical layers were used for the quarter WP model.

Figure 4-2 presents detailed views of the quarter WP shale model as rendered in Cubit software. The left panel displays all volumes associated with the model in and around the WP region. The middle panel includes both the volumes and the mesh of the model, providing a comprehensive overview of its structure. The right panel features the Cubit mesh quality metric set to Scaled Jacobian, highlighting a few lower-quality cells in the drift region. However, these cells remain within the generally acceptable range, as values above 0.6 are typically considered satisfactory. Figure 4-3 provides a close-up view of the mesh in the region in and around the waste package.

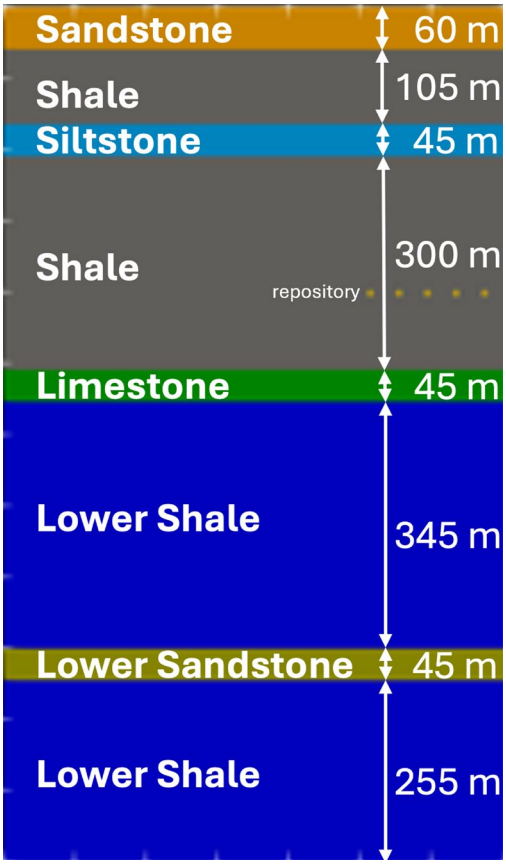

Figure 4-1. Vertical view of the model domain for the shale case, spanning 1200 m depth. (LaForce et al., 2024) Colored and Labeled by Material Showing Specified Thicknesses for the Full Vertical Extent. The same vertical layer structure was used for the quarter WP shale model.

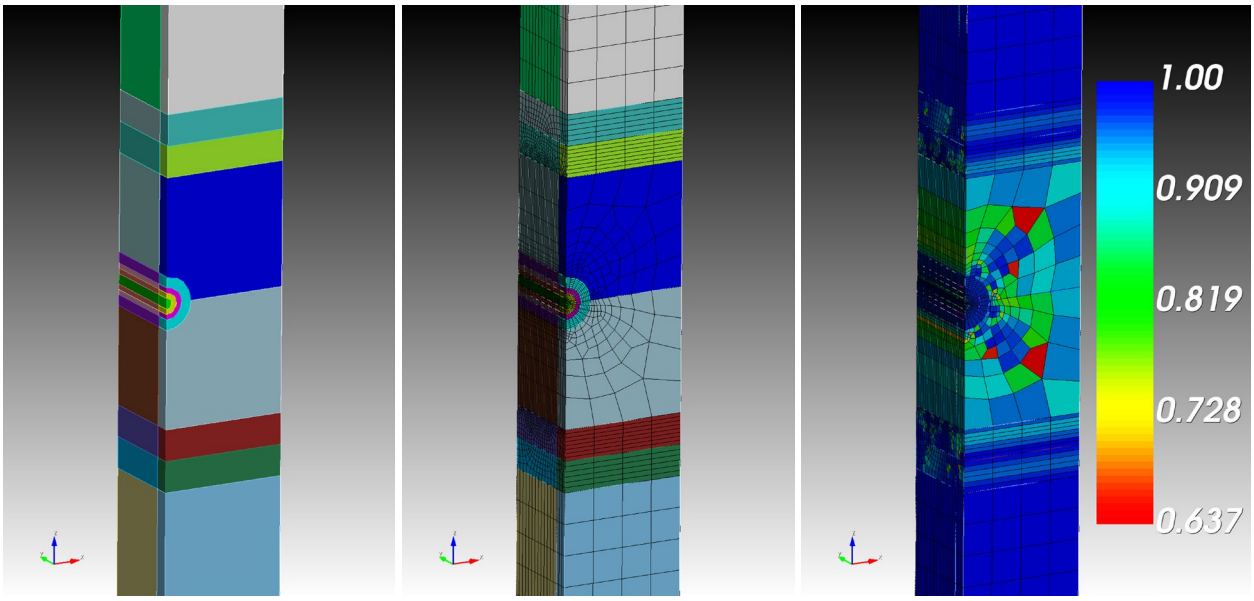

Figure 4-2. Zoomed-in visuals of the quarter WP shale model within the Cubit software are presented as follows: 1) Left: A view displaying all volumes associated with the model in and around the WP region; 2) Middle: A view showcasing all volumes along with the mesh of the model; 3) Right: A representation of the Cubit mesh quality metric set to Scaled Jacobian.

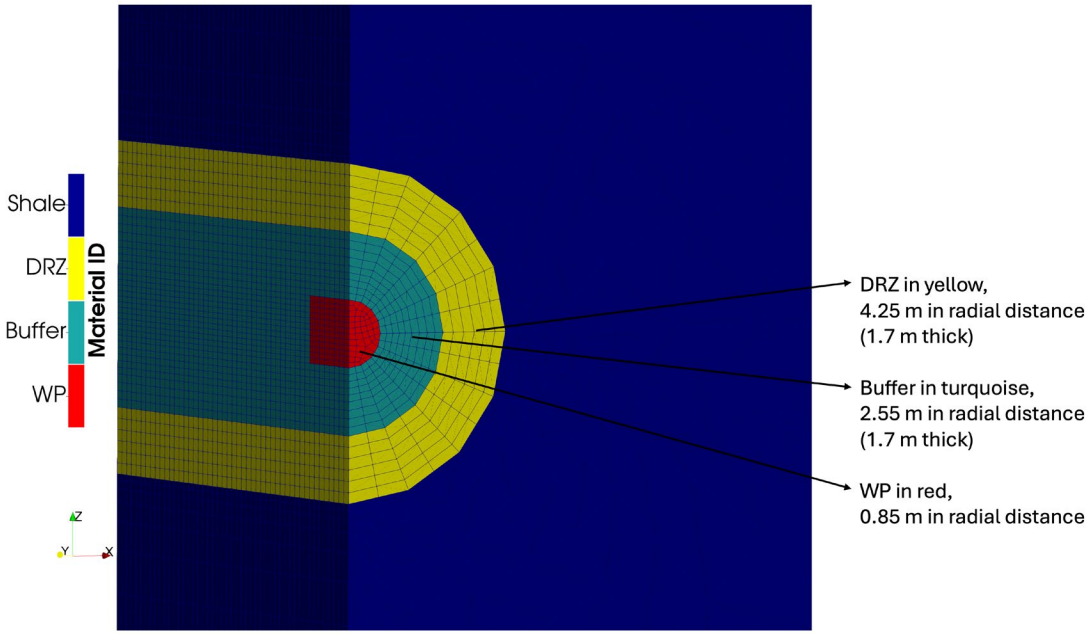

Figure 4-3. Close-up of meshed regions of interest within the quarter WP shale model.

Five base case PFLOTRAN simulations were run to test the initial workflow and the model. These simulations are configured to operate with a subsurface flow process model, focusing specifically on the effects of pressure and temperature resulting from varying model parameters, without considering transport processes. Boundary conditions are applied solely at the top and bottom of the model, while the north, west, south, and east boundaries are treated as reflective. This approach effectively simulates an infinite array of waste packages.

The initial gas saturations were set at 28.5% for the DRZ and 70% for both the buffer and WP. The base case simulations were executed over a period of one million years using PFLOTRAN. We developed an approach to generate generic heat output curves representing the thermal output of the spent nuclear fuel that can be scaled to represent a wide range of inventory SNF (Basurto, et al., 2025). The decay heat in these base case simulations was varied. The simulation results for these five base case scenarios indicate that the highest calculated temperature at the WP was 209°C, occurring in Run 5. This finding is consistent with expectations, as Run 5 featured the highest initial WP wattage of 1750 W. Furthermore, Run 5 also exhibited the highest maximum pressure of 6.47 MPa at the WP, and dry out was observed in the WP region.

Visualizations were generated in ParaView. For a complete set of visualizations, see (Basurto, et al., 2025). In this report, we show one example of the visualizations in Figure 4-4, which displays 70-year illustrations colored by Material ID, Temperature (°C), Maximum Pressure (Pa), Liquid Saturation, and additionally time series in the WP (red), buffer (turquoise), DRZ (yellow) and shale (dark blue). Note that the time series indicate that the maximum temperature of 209°C has been reached at the waste package region by year 10 and dry out can be seen as well. Figure 4-4H shows that liquid saturation in the waste package falls to zero very early in the simulation (~ year 1) and begins to resaturate after about year 1000. By year 70, the maximum pressure of 6.47 MPa is reached at the waste package (Figure 4-4G). This illustration is just one example: the full ensemble of simulations performed for sensitivity analysis is described in Section 4.2.

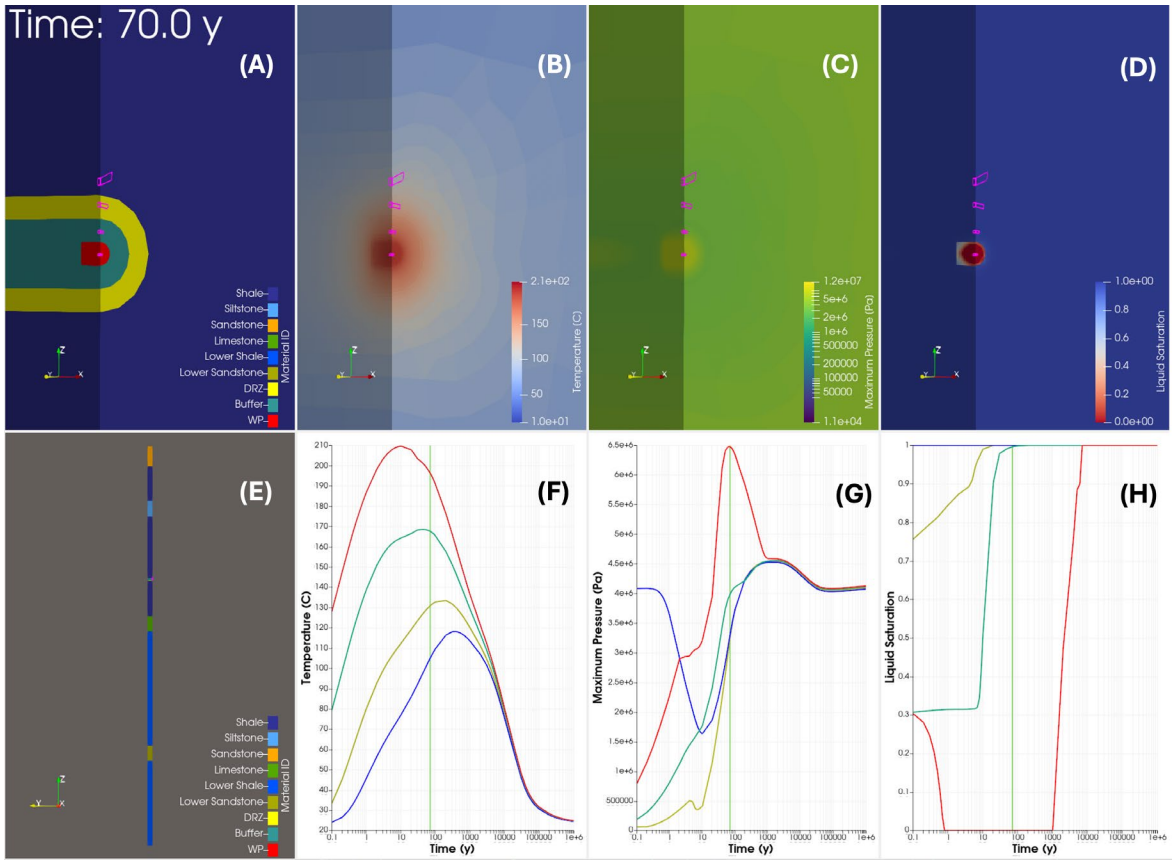

Figure 4-4. Simulation results for Run 5 at year 70, illustrating the nearfield with the following color-coded quantities: (A) Material ID, (B) Temperature [°C], (C) Maximum Pressure [Pa], and (D) Liquid Saturation. Additionally, (E) provides a full view of the quarter WP model, colored by Material ID. The three line plots depict observations over the entire one-million-year simulation at the WP (red), buffer (turquoise), DRZ (yellow), and Shale (dark blue) for (F) Temperature [°C], (G) Maximum Pressure [Pa], and (H) Liquid Saturation.

4.2 SENSITIVITY ANALYSIS: INPUT PARAMETERS AND OUTPUT QOIS

This section describes the uncertain input parameters and the output quantities of interest that were analyzed as part of a 200-sample study on the quarter WP shale reference case. While the base case simulations were executed over a period of one million years using PFLOTRAN, simulations in the 200-sample study were set with a final time of 50,000 years. In the 2024 full shale generic reference case, nine epistemic parameters were treated as uncertain and independent: see (Swiler L. P., et al., 2024), Section 4.1 for details. These are PFLOTRAN variables that were selected and implemented as uncertain parameters in the Next Gen Workflow (NGW). In the quarter shale case study, we varied 10 parameters as described in Table 4-1. The parameters are uncorrelated. Correlations between input parameters are not included because an evidence-based correlation structure has not been developed.

The shale permeability anisotropy ratio is the ratio of the shale permeability in the vertical direction to the shale permeability in the horizontal direction. When this ratio is low, it indicates greater horizontal than vertical permeability (more anisotropic permeability). When the ratio is 1, it indicates the same horizontal and vertical permeability. The shale thermal conductivity anisotropy ratio is similar, except that it compares the thermal conductivity between the vertical and horizontal directions. Low values indicate more horizontal than thermal conductivity in the shale and when the value is 1, the thermal conductivity in the shale is the same in the vertical and horizontal directions.

Table 4-1 Input parameter distributions for the quarter shale reference case.

Input	Description	Range	Units	Distribution
pShale	Host Rock (Shale) Porosity	0.1 – 0.25	-	uniform
pBuffer	Buffer Porosity	0.3 – 0.5	-	uniform
pDRZ	DRZ Porosity	0.05 – 0.25	-	uniform
kShale	Host rock (shale) Permeability	10^{-20} – 10^{-17}	m^2	log uniform
kBuffer	Buffer Permeability	10^{-20} – 10^{-16}	m^2	log uniform
kDRZ	DRZ Permeability	10^{-18} – 10^{-16}	m^2	log uniform
TK_buffer_wet	Thermal conductivity of buffer (wet). *Note dry TK = 0.5 * wet.	1.2 - 3.0	W/(K-m)	uniform
TK_shale_drz_wet	Thermal conductivity of shale and DRZ (wet). *Note dry TK = 0.5 * wet.	0.68 - 1.42	W/(K-m)	uniform
k_ani_shale	Shale permeability anisotropy ratio	0.1, 0.5, or 1.0	-	discrete values
TK_ani_shale	Shale thermal conductivity anisotropy ratio	0.1, 0.5, or 1.0	-	discrete values

We generated 200 samples of these input parameters using LHS and ran the PFLOTRAN quarter WP shale reference case model to obtain the QoIs. The QoIs are shown in Table 4-2. All QoIs were calculated at observation points at the WP, buffer in both horizontal directions, DRZ in the x-direction, shale in z-and x-directions, and observation points vertically in the lower sandstone, limestone, shale, silt, and upper sandstone.

Table 4-2 Quantities of Interest for the quarter shale reference case

Quantity of Interest	Description
Maximum Pressure	Maximum over time of the liquid and gas pressure [Pa] at a fixed observation point
Maximum Temperature	Maximum over time of the temperature at a fixed observation point [$°C$]
Liquid Saturation	Liquid saturation at a fixed time and observation point, expressed as a proportion between 0 and 1 of the pore space within the rock that is filled with liquid

4.3 SENSITIVITY ANALYSIS RESULTS

This section discusses sensitivity analysis results for the shale repository reference case. We note that of the 200 PFLOTRAN simulations, 195 completed successfully. The others had parameter combinations that resulted in computationally infeasible runs with very rapid dry out. This study still provided enough completed simulations (195) compared to the dimension of the input space (10) for Sobol' index estimation to be feasible. In analyses for previous cases, we have used multiple types of surrogate models to estimate Sobol' indices with a preference for polynomial chaos expansion (PCE) models when such a model fits the simulation data well. This is because PCE models are flexible with respect to input/output relationships and allow direct calculation of the Sobol' indices via the expansion model coefficients. PCE models cannot be fit with discrete variables, however, and the anisotropy input variables (k_ani_shale and TK_ani_shale) in this quarter scale shale model are discrete. A discrete distribution was chosen between three equally weighted outcomes due to a lack of information for an empirical distribution. The three values covered by the discrete distribution capture the assumption (a value of 1.0) from the FY24 Shale case analysis, a typical assumption for sedimentary systems (0.1), and a middle value (0.5). To allow for surrogate model construction given these discrete distributions, we chose second-order polynomial regression models to estimate the Sobol' indices. With this type of surrogate model, the Sobol' indices are not calculated. Rather, the surrogate model is sampled many times and the Sobol' indices are approximated from the samples. For these results we used LHS sampling on the polynomial surrogate models with 5000 samples for the Sobol' estimates.

Sensitivity analysis was performed for the maximum values (over time) of the quantities of interest at each of the observation points shown in Figure 4-5. Because results are very similar for many of the observation points, only some of the results are included here, and we note at which observation points the sensitivity conclusions are the same. Observation points that are explicitly shown are discussed by location, starting at the waste package, moving in the x-direction, then the y-direction, and then the z-direction for each quantity of interest. Results are not included for the liquid saturation quantity of interest because the maximum over time of the liquid saturation is 1 for all simulations and observations. Plots of the time-dependent liquid saturation are discussed for qualitative sensitivity analysis conclusions.

For time-dependent discussion, we only present qualitative graphical results in the form of time series plots of the quantities of interest colored by influencing input variables.

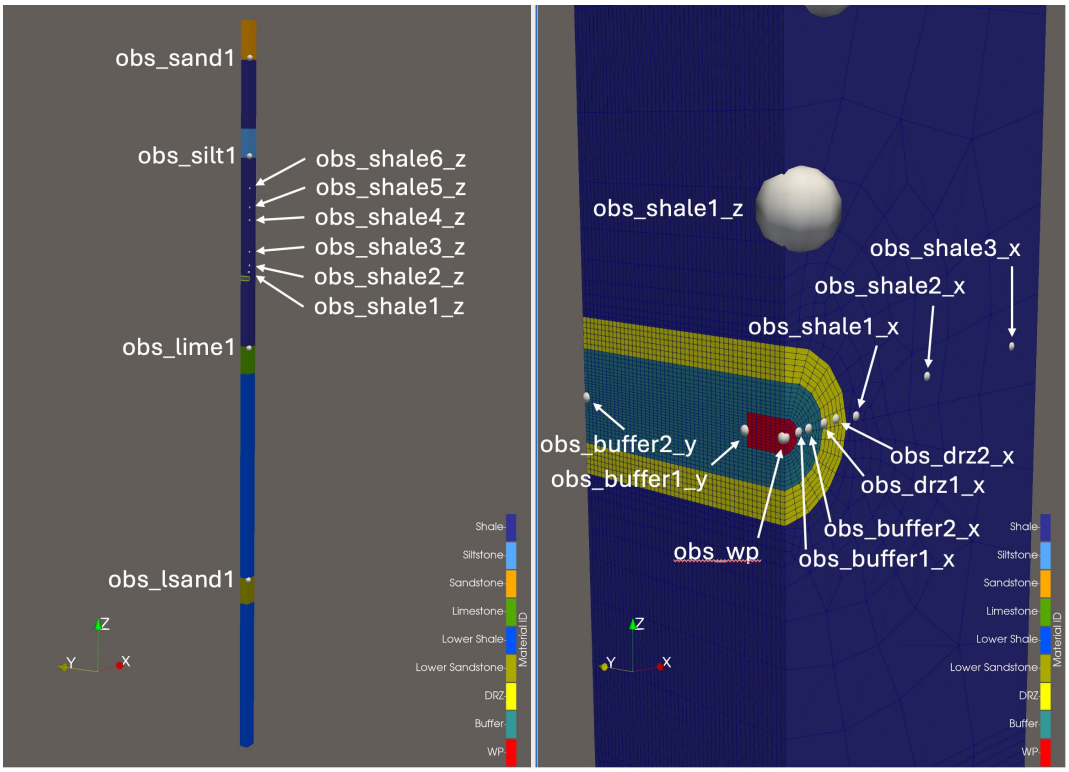

Figure 4-5 The left of the figure shows observation points within the z-direction; the right of the figure shows observation points around the central waste package.

4.3.1 TEMPERATURE

Sobol' indices for the maximum temperature over time at the waste package observation point are shown in Figure 4-6. The total effect indices and main effect indices are similar, indicating few interaction effects. The thermal conductivity parameters are all significant for this quantity of interest (QoI) and no other parameters appear to have a significant effect at this observation point. These effects make sense. Higher values of the shale thermal conductivity anisotropy ratio parameter (TK_ani_shale) correspond to lower anisotropy which results in higher effective conductivity around the drift, thus lower temperatures at the waste package. The thermal conductivity parameters in the shale, DRZ, and buffer all have a negative correlation with waste package temperature; lower thermal conductivity in the regions surrounding the waste package maintains higher temperatures at the waste package.

Sobol' indices for the maximum temperature at observation points 1 and 2 in the buffer in the x-direction are shown in Figure 4-7. Closest to the waste package (left), the results are similar to the results at the waste package observation point. Farther from the waste package, the shale thermal conductivity anisotropy ratio dominates the results and the thermal conductivity of the shale and the DRZ becomes more important than that of the buffer. Dominance of the shale thermal conductivity anisotropy farther from the waste package makes sense because the domain has much more shale than buffer and DRZ material.

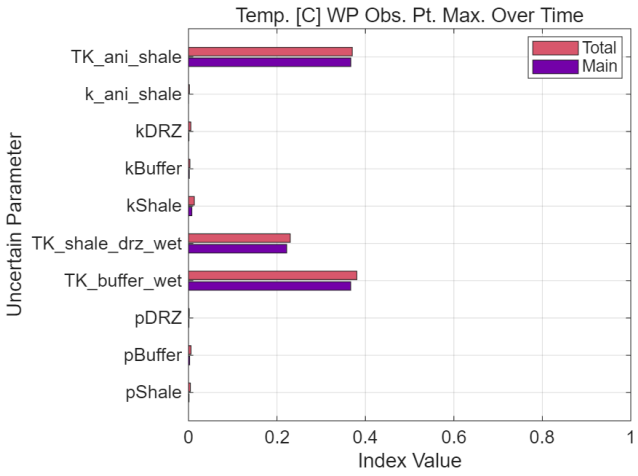

Figure 4-6 Maximum temperature Sobol' indices at the waste package observation point

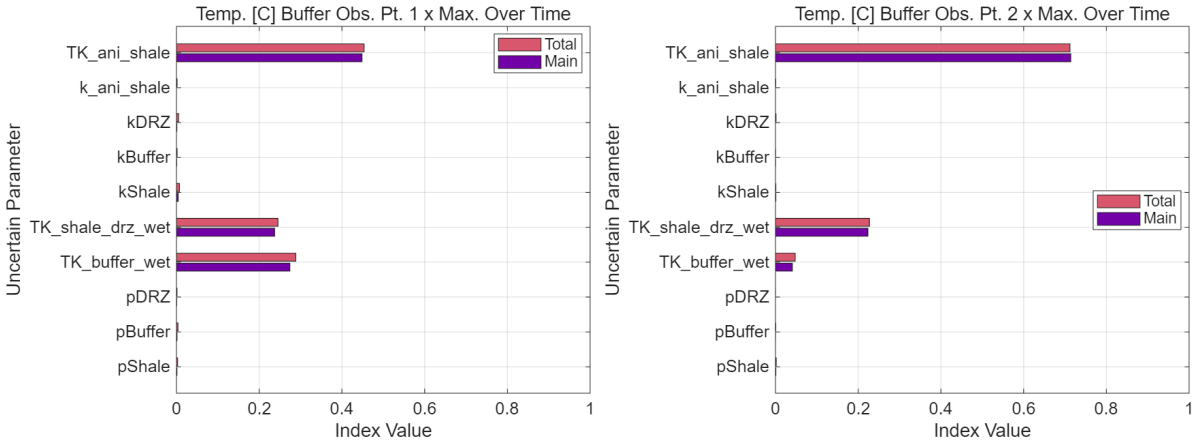

Figure 4-7 Maximum temperature Sobol' indices at lower buffer observation point 1 in the x-direction (left figure) and buffer observation point 2 in the x-direction (right figure)

Sobol' indices for the maximum temperature at the first observation point in the DRZ and the last observation point in the shale (in the x-direction) are shown in Figure 4-8. These figures show increasing importance of the shale thermal conductivity anisotropy ratio and decreasing importance of the thermal conductivity of the shale and the DRZ at observation point farther in the x-direction. Only one point is shown each in the DRZ and shale because the other DRZ and shale observation points have the same interpretation. By these observation points, more than 80% of the variance is accounted for by the shale thermal conductivity anisotropy. The buffer thermal conductivity no longer has a significant effect at the first observation point in the DRZ and the DRZ/shale thermal conductivity no longer has a significant effect at observation points within the shale.

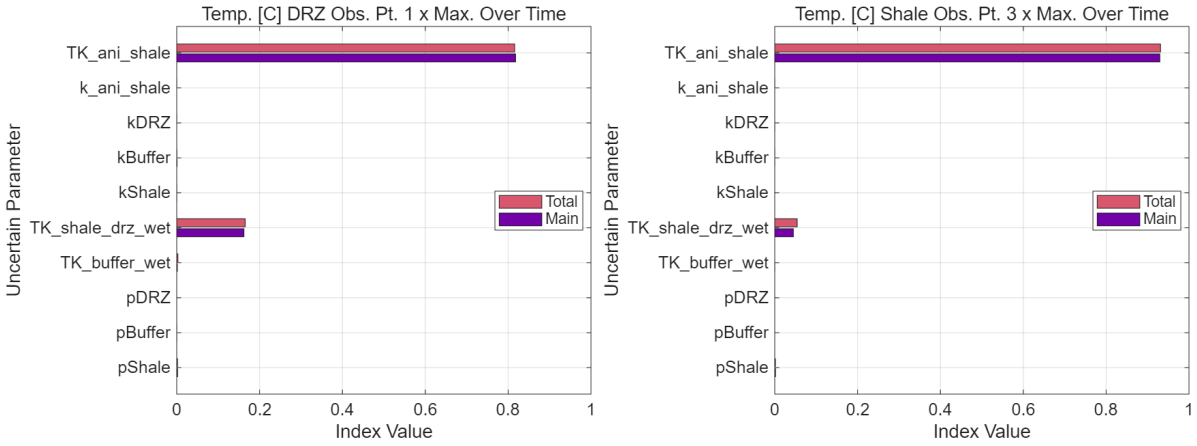

Figure 4-8 Maximum temperature Sobol' indices at DRZ observation point 1 (left figure) and shale observation point 3 in the x-direction (right figure)

Scatterplots support the Sobol' index conclusions. The scatterplots in Figure 4-9 show the maximum temperature at the waste package observation point plotted versus the input parameters. The purple points in the scatterplots are the simulation results. The orange points in the plots are the results from the surrogate second-order polynomial evaluated at the same input parameter values. These plots help confirm the input/output relationships in the Sobol' index results and the matching trends between the simulation and surrogate points demonstrate the surrogate quality. This scatterplot confirms the directionality of the input/output relationships; higher thermal conductivities result in lower temperatures at the waste package and higher thermal conductivity anisotropy ratios (more uniform thermal conductivity) also result in lower temperatures at the waste package.

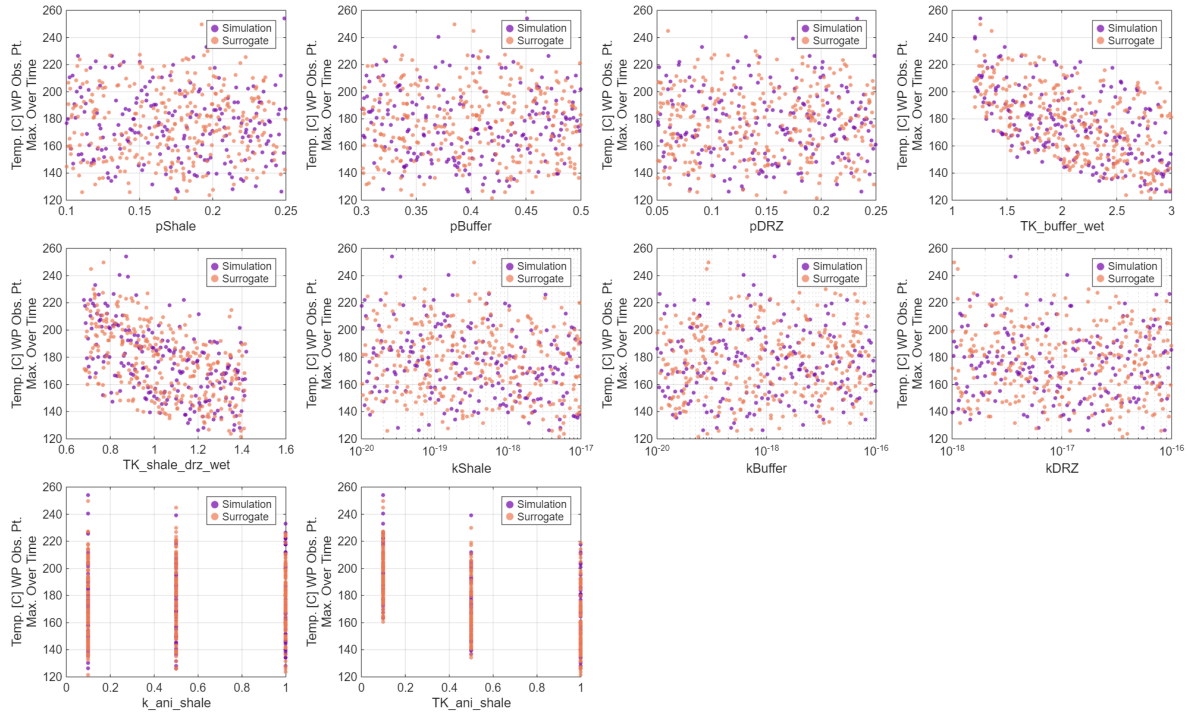

Figure 4-9 Scatterplots for the maximum temperature at the waste package observation point

The scatterplots in Figure 4-10 through Figure 4-12 show the maximum temperature input/output relationships in the x-direction at buffer observation point 1, buffer observation point 2, and shale observation point 3.

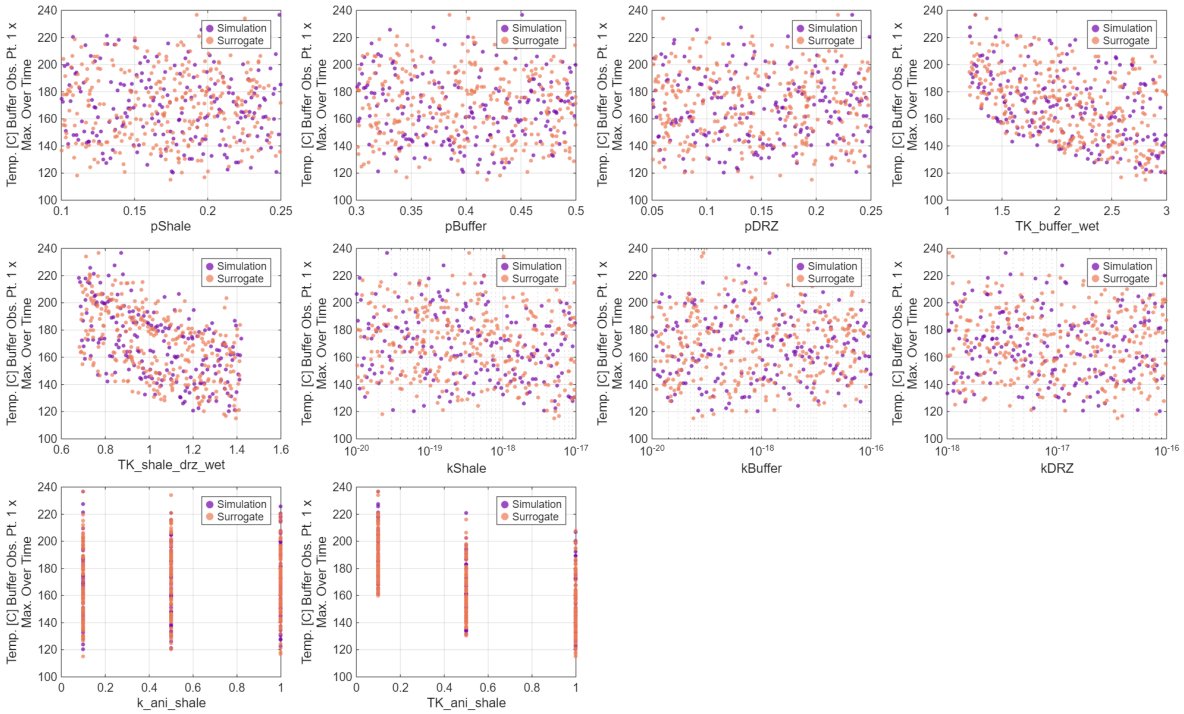

Figure 4-10 Scatterplots for the maximum temperature at buffer observation point 1 in the x-direction

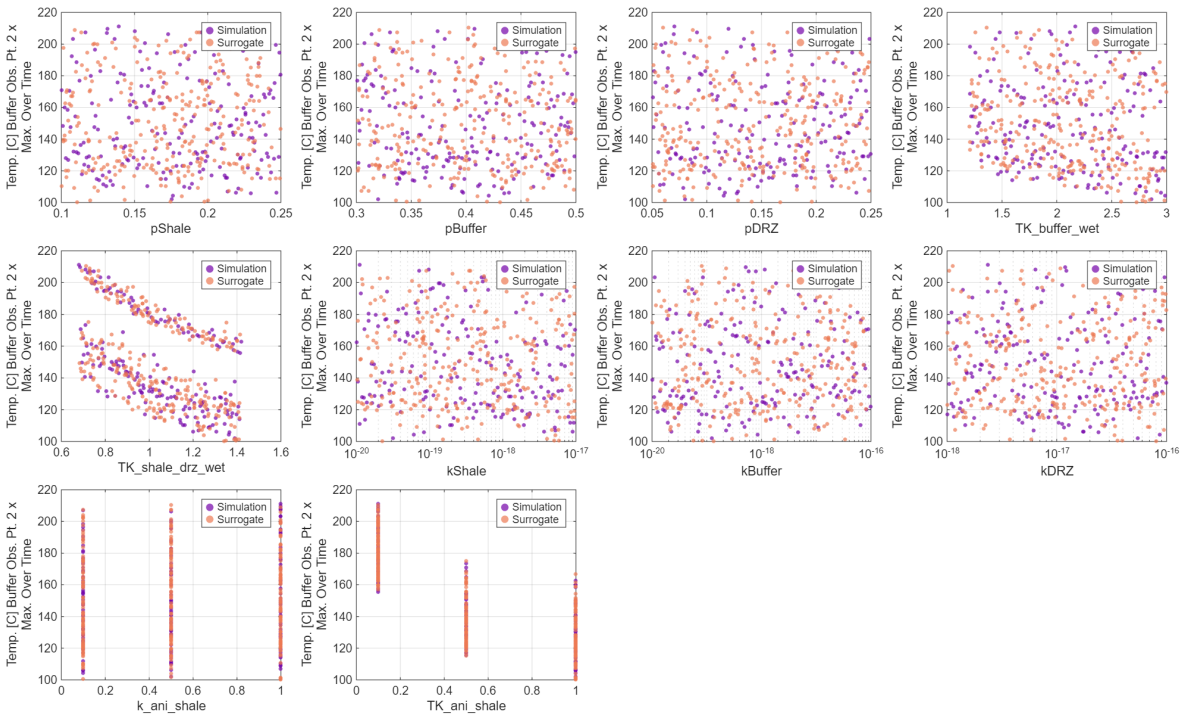

Figure 4-11 Scatterplots for the maximum temperature at buffer observation point 2 in the x-direction

Comparison between the buffer observation points (Figure 4-10 and Figure 4-11) illustrates why the Sobol' index results differ between these observation points. At observation point 1, TK_ani_shale has a slight effect, but the most noticeable trends are with respect to TK_buffer_wet and TK_shale_DRZ_wet. At observation point 2, TK_buffer_wet has a significantly diminished effect on the maximum temperature. However, TK_ani_shale and TK_shale_drz_wet both have much more pronounced effects, which are actually an interaction effect. This effect is also seen in Figure 4-12. TK_ani_shale causes a bifurcation in the maximum temperature at shale observation point 3 in the x-direction. The three values for TK_ani_shale correspond to the three clusters of points in the plot of temperature versus TK_shale_drz_wet. In essence, the shale thermal conductivity anisotropy ratio determines whether the maximum temperature will be on average below 80°C, around 90°C, or around 160°C. Variation around this average value is then determined by the thermal conductivity of the shale and DRZ. The bifurcation of points into a high temperature population and a low temperature population is controlled by the thermal conductivity anisotropy ratio; there is no overlap in temperature at this observation point between simulations with the ratio set to 0.1 and simulations with the ratio set to either 0.5 or 1. Observation point 2 sees less distinct clustering, especially between realizations with thermal conductivity anisotropy ratios of 0.5 and 1 because the trend with respect to TK_ani_shale is weaker. Farther from the waste package, a higher anisotropy ratio allows heat to spread more uniformly in all directions, reducing sensitivity to changes in thermal conductivity. At the lowest anisotropy ratio, heat spreads less uniformly, which is why the cluster of points with the lowest anisotropy ratio is still relatively highly sensitive to thermal conductivity at observation point 3.

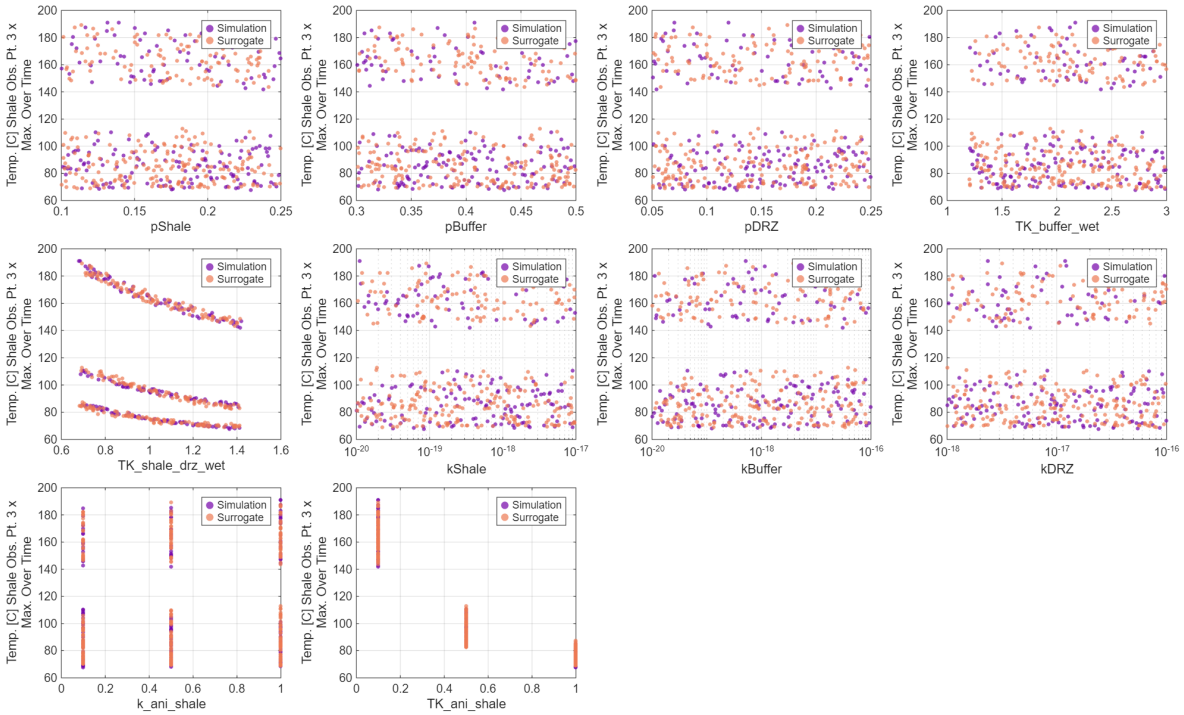

Figure 4-12 Scatterplots for the maximum temperature at shale observation point 3 in the x-direction

Time series plots of the temperature at the waste package observation point are shown in Figure 4-13 colored by TK_ani_shale (left), TK_buffer_wet (center), and TK_shale_drz_wet (right). These plots show the effect of the thermal conductivity in the buffer (closest to the observation point) early in the simulation and the effect of the thermal conductivity in the DRZ and shale (further from the observation point) later in the simulation, which make sense. Additionally, note the clustering of simulations, especially late, with respect to the shale thermal conductivity anisotropy ratio (left). This is the same effect we observed in the scatterplots; the anisotropy determines the whether the temperature is low

or high, on average. Observe in the plot on the right that within each cluster, the temperature is negatively correlated with the thermal conductivity of the shale and the DRZ. As we saw with the maximum temperatures farther from the waste package, we see interaction between the shale thermal conductivity anisotropy ratio and other thermal conductivity parameters for late-simulation temperatures at the waste package. Greater anisotropy (a lower anisotropy ratio) lowers effective thermal conductivity around the drift. This results in a cluster of realizations with higher overall temperatures and the temperature at the waste package decreases more slowly. For these realizations, if the thermal conductivity in the DRZ and shale are also low, this further slows cooling, explaining the interaction effect between the two parameters (Figure 4-13 right).

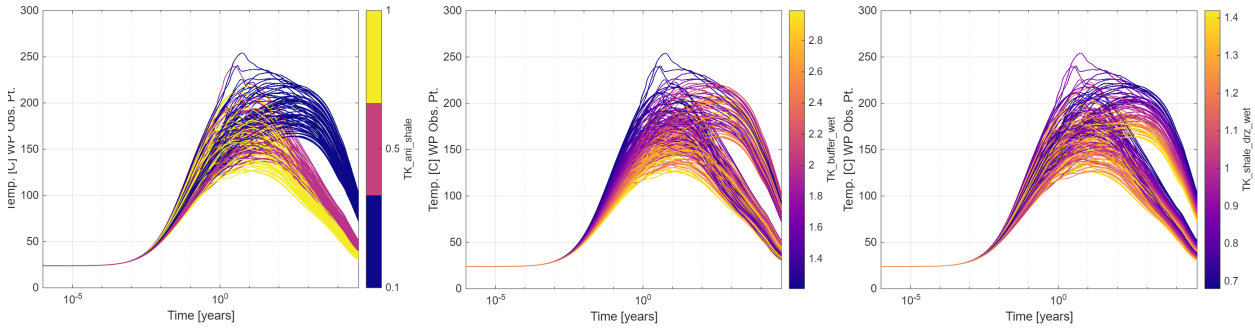

Figure 4-13 Time series plots of the temperature at the waste package observation point colored by the shale thermal conductivity anisotropy ratio (left), thermal conductivity of the buffer (center), and thermal conductivity of the shale and DRZ (right)

Time series plots of the temperature at DRZ observation point 1 and shale observation point 3 (both in the x-direction) are plotted in Figure 4-14 and Figure 4-15. In both cases, coloration of the time series by TK_ani_shale (left) and TK_shale_drz_wet (right) shows the same interaction effect as was observed at the waste package. However, as the observation point moves farther into the shale, the effect of the shale thermal conductivity anisotropy ratio becomes even more pronounced. These time series results are also consistent with the maximum temperature Sobol' index results at these observation points; no other parameters had significant Sobol' indices at these observation points and no other parameters had clear effects when used to color the time series plots.

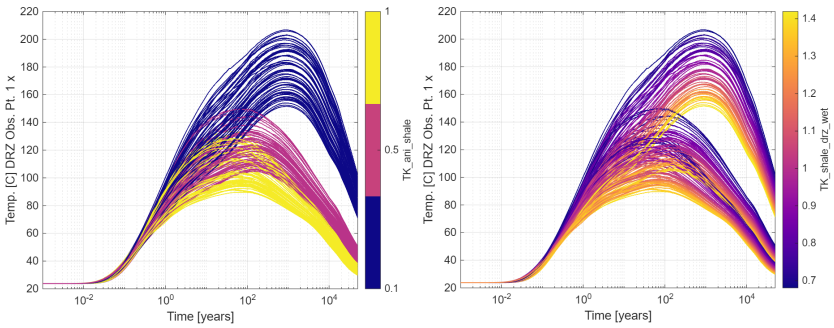

Figure 4-14 Time series plots of the temperature at DRZ observation point 1 in the x-direction colored by the shale thermal conductivity anisotropy ratio (left) and thermal conductivity of the shale and DRZ (right)

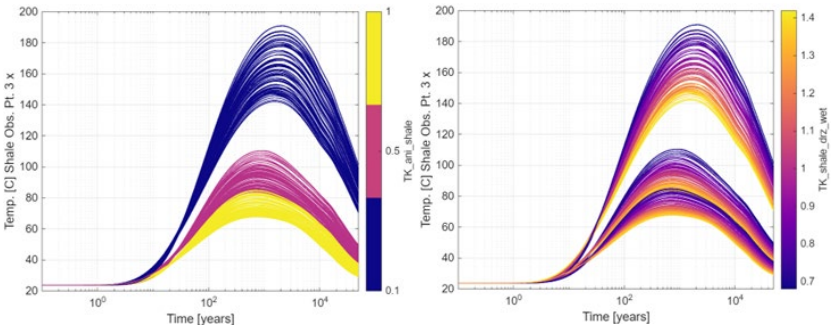

Figure 4-15 Time series plots of the temperature at shale observation point 3 in the x-direction colored by the shale thermal conductivity anisotropy ratio (left) and thermal conductivity of the shale and DRZ (right)

There are only two observation points located along the y-direction from the waste package, both in the buffer. Sobol' indices at these observation points are shown in Figure 4-16. These results are very similar to those in the x-direction. Near the waste package, the shale thermal conductivity anisotropy ratio is the most important parameter and the thermal conductivity within the buffer and DRZ and shale are also significant. At the second observation point farther away, the shale thermal conductivity anisotropy ratio dominates the results. Usually a Sobol' index less than 0.1 would be considered suspect; it is not necessarily spurious but could be. In this case, however, scatterplots suggest the Sobol' indices for TK_shale_DRZ_wet at observation point 2 in the buffer (y-direction) are meaningful, though small.

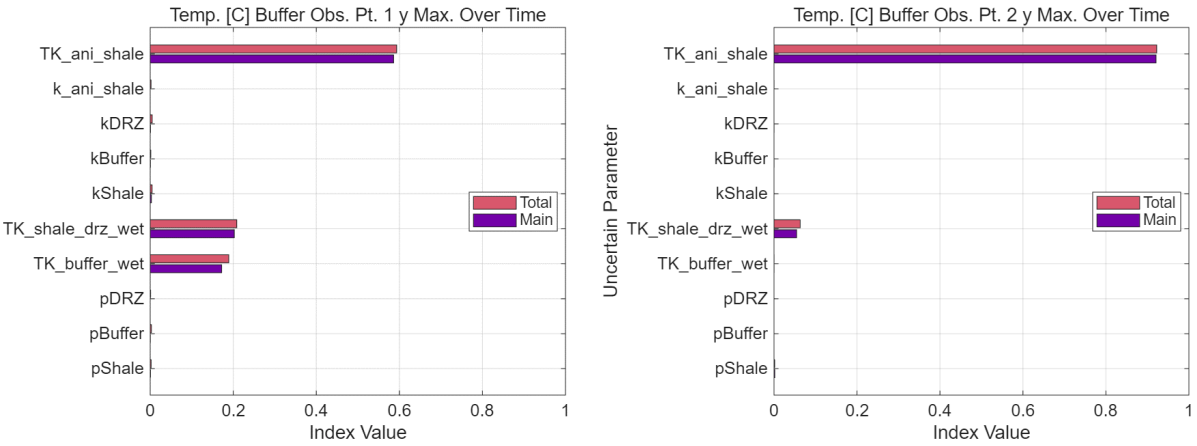

Figure 4-16 Maximum temperature Sobol' indices at buffer observation point 1 in the y-direction (left figure) and buffer observation point 2 in the y-direction (right figure)

Scatterplots for the first observation point do not provide addition insights beyond those already discussed because of the similarity to the analysis in the x-direction, so only the scatterplots at observation point 2 are included here, in Figure 4-17. We see the same interaction effect between TK_ani_shale and TK_shale_drz_wet as observed in the x-direction analysis. Note that the negative slopes with respect to TK_shale_drz_wet appear significant, also as in the x-direction. This is a meaningful relationship, despite the small Sobol' index in Figure 4-16. It is also notable that this is an interaction effect and there is very little difference between the main and total effect Sobol' indices. Even though the scatterplots show good performance of the order 2 polynomial surrogate model, this is an inconsistency between the graphical analysis and the Sobol' index analysis. Time series plots in

the y-direction yield the same insights as those in the x-direction, so no time-series plots are included here.

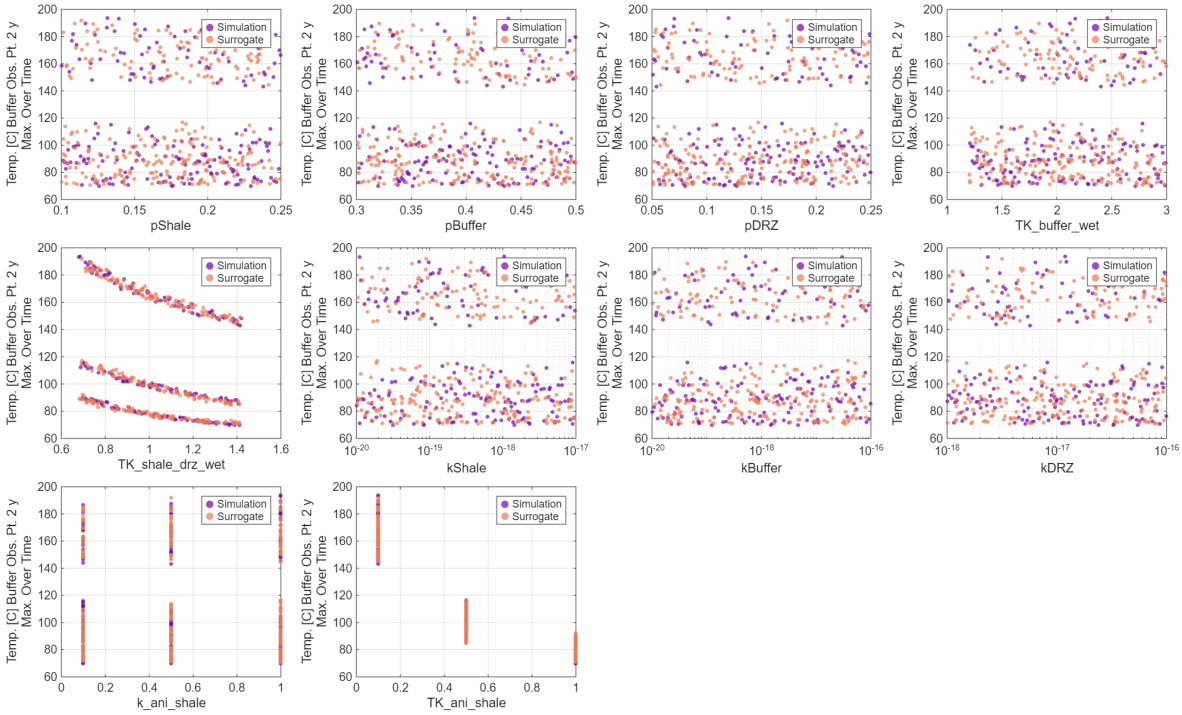

Figure 4-17 Scatterplots for the maximum temperature at observation point 2 in the buffer in the y-direction

There are ten observation points in the z-direction, however, there is little variation in results between these observation points. As such, we only present results for the lowest and topmost layers (lower sandstone observation point 1 and sandstone observation point 1), in Figure 4-18. The shale thermal conductivity anisotropy ratio is the dominant parameter at both observation points and the shale and DRZ thermal conductivity parameter has secondary importance. At the topmost observation point, TK_shale_drz_wet accounts for almost 20% of the variance including the interaction effect with TK_ani_shale.

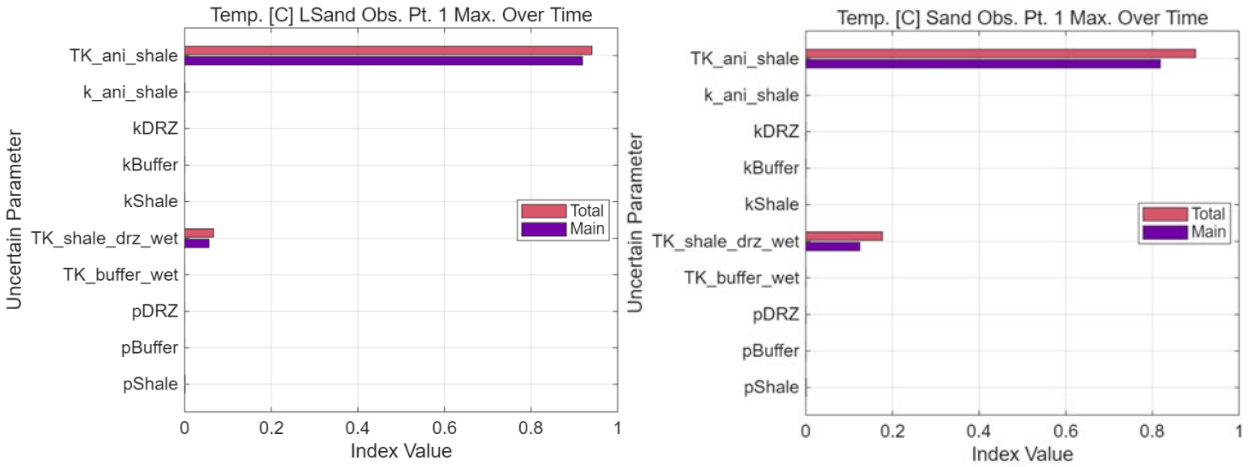

Figure 4-18 Maximum temperature Sobol' indices at lower sandstone observation point 1 (left figure) and sandstone observation point 1 (right figure)

Comparing the scatterplots in Figure 4-19 and Figure 4-20, we see a different behavior at the topmost observation point than at all other observation points. In Figure 4-19 we see the same negative correlations between TK_ani_shale and temperature and TK_shale_drz_wet and temperature as at observation point around the waste package. However, at the topmost observation point (Figure 4-20), both correlations are positive. Notice, however, that the maximum temperatures are low with very little variation at the topmost observation point. The interaction effect is limited to those realizations for which the thermal conductivity is high enough that the temperature disturbance actually reaches this observation point. For lower values of TK_ani_shale, the thermal conductivity in the z-direction is lower, so fewer realizations result in elevated temperatures at sandstone observation point 1. For higher values of TK_ani_shale, the thermal conductivity in the z-direction is high enough for some heat to reach the upper sandstone observation point. The temperature will be higher here with higher thermal conductivity in the z-direction through the DRZ and shale, hence the effect from TK_shale_drz_wet.

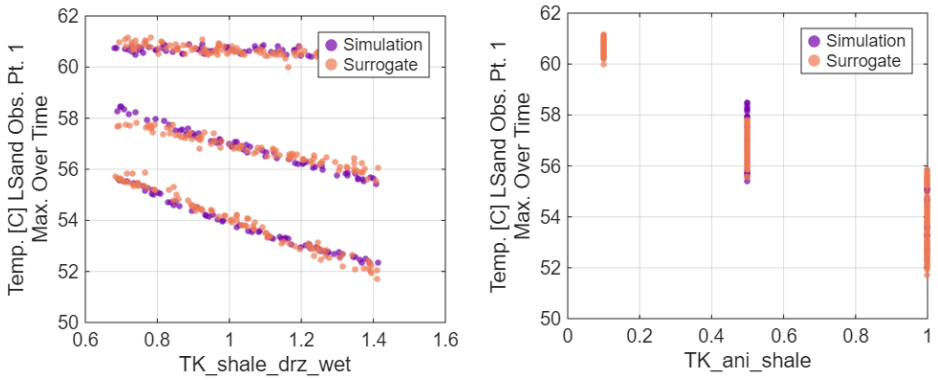

Figure 4-19 Scatterplots of the maximum temperature at lower sandstone observation point 1 versus TK_shale_drz_wet (left) and TK_ani_shale (right)

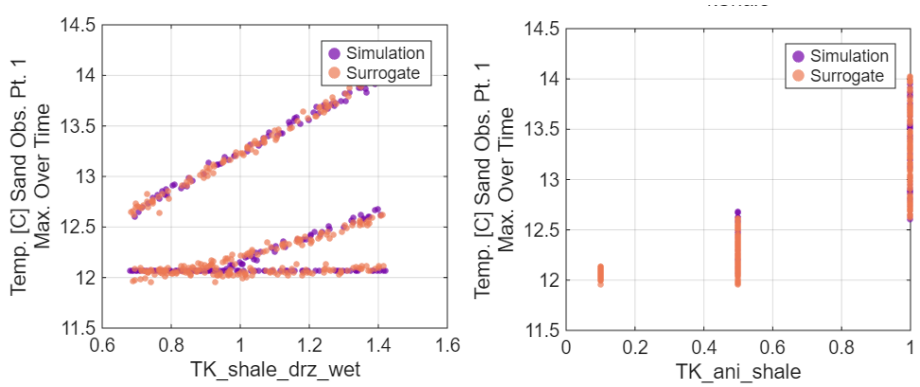

Figure 4-20 Scatterplots of the maximum temperature at upper sandstone observation point 1 versus TK_shale_drz_wet (left) and TK_ani_shale (right)

These behaviors are also observed in the time series data. The time series data are plotted in Figure 4-21 for the lower sandstone observation point (top) and upper sandstone observation point (bottom). The interaction effects in the top plot, wherein each TK_ani_shale cluster of realizations has a strong negative correlation pattern with the TK_shale_drz_wet color scale, are the opposite of the interaction effects in the bottom plot.

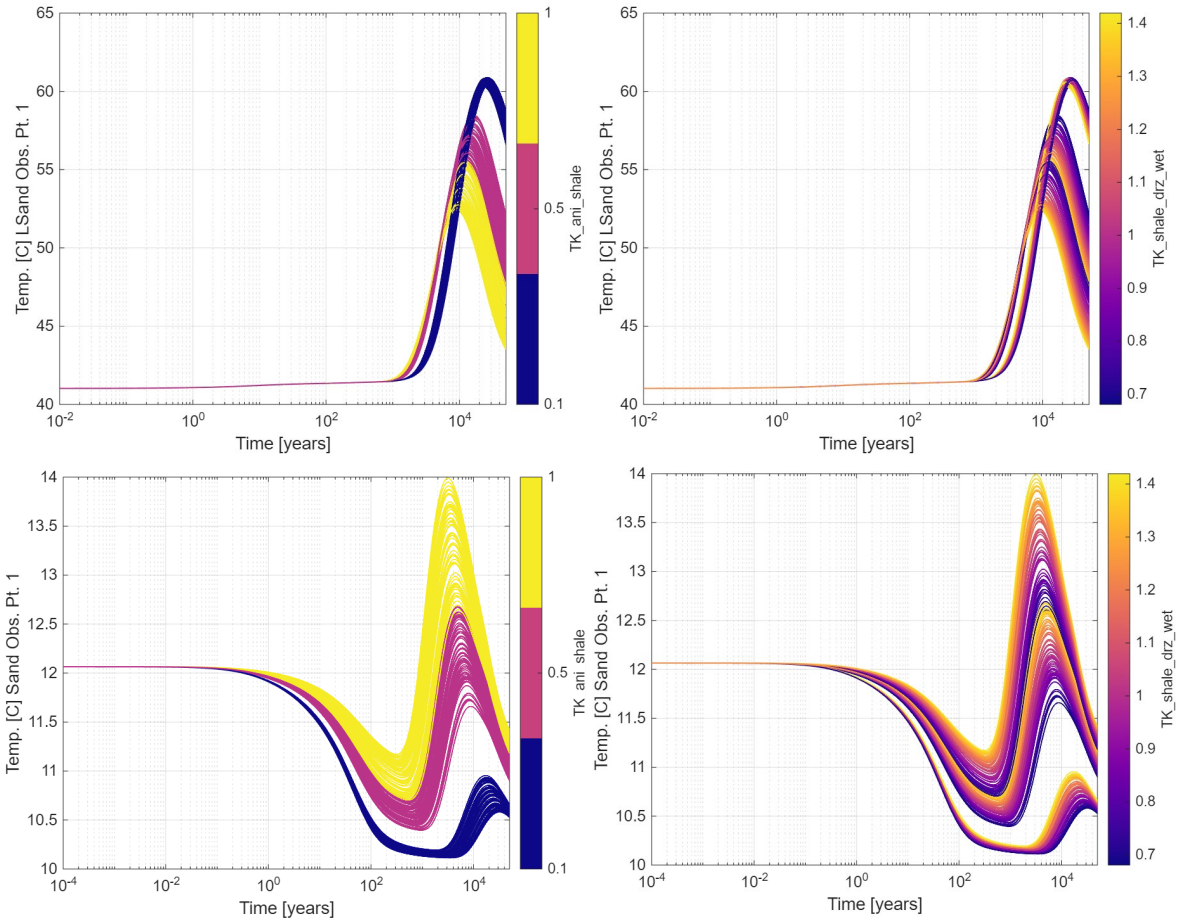

Figure 4-21 Time series plots of the temperature colored by the shale thermal conductivity anisotropy ratio (left) and thermal conductivity of the shale and DRZ (right) at lower sandstone observation point 1 (top figures) and upper sandstone observation point 1 (bottom figures)

4.3.2 PRESSURE

This section present sensitivity analysis results for the pressure. Some of these results are more challenging to interpret than the temperature results because the relationships are less clear in scatterplots and time series plots and there are more parameters with nonzero Sobol' indices.

Sobol' index results for the maximum pressure at the waste package observation point (left) and shale observation point 3 in the x-direction are shown in Figure 4-22. The corresponding scatterplots are in Figure 4-23 and Figure 4-24. Though the scatterplots show generally good agreement between the simulation and the surrogate, the Sobol' index results at the waste package observation point are suggestive of overfitting because of the nonzero total effect indices on all parameters. While this is not impossible, we often see this type of behavior in results where the surrogate model is overfit so the total effect indices should be interpreted with caution. The R^2 for this model is also 0.77, which is relatively low compared to most of the other observation points which have R^2 values over 0.9 (1.0 being a perfect fit). As in the maximum temperature results, TK_ani_shale is also the dominant uncertainty for maximum pressure at the waste package observation point. The main effect indices for TK_shale_drz_wet, TK_buffer_wet_and kBuffer are also potentially significant.

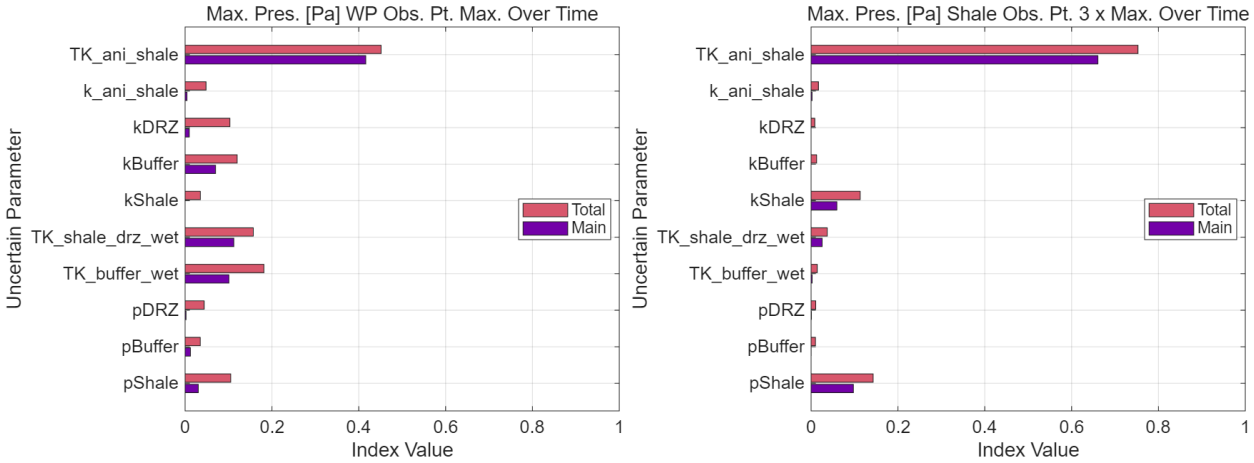

Figure 4-22 Maximum pressure Sobol' indices at the waste package observation point (left figure) and shale observation point 3 in the x-direction (right figure)

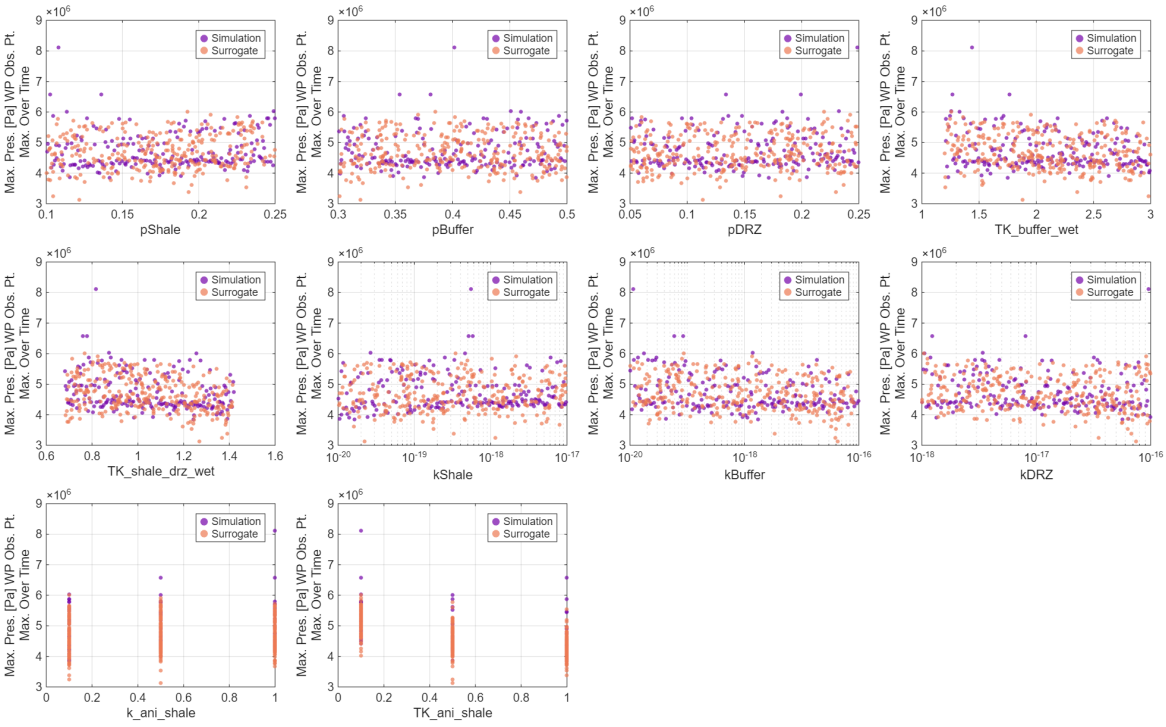

Figure 4-23 Scatterplots for the maximum pressure at the waste package observation point

The Sobol' index results become clearer farther from the waste package. At shale observation point 3 in the x-direction (Figure 4-22, right), there appear to be three significant parameters: TK_ani_shale, kShale, and pShale. These results are also much clearer in the scatter plots (Figure 4-24) than the waste package observation point pressure results were. Within the shale, maximum pressure is driven predominantly by the shale thermal conductivity anisotropy ratio and secondarily by the porosity and permeability of the shale. Because the anisotropy ratio drives temperature variability at this observation point, it makes sense that it would also affect the pressure. The negative correlation with kShale also make sense with higher permeability preventing as much pressure from building up. The relationship between pShale and pressure does not have a clear intuitive explanation; it is unclear why

higher porosity would increase pressure. However, see Figure 4-25, which shows the plot of maximum pressure at this observation point versus pShale colored by kShale. The points that comprise the stronger positive trend with respect to porosity also have low permeability values. It is the combination of high porosity with low permeability that creates this positive trend. This does not fully explain the positive trend with respect to pShale as there is still a slight positive trend even at higher kShale values.

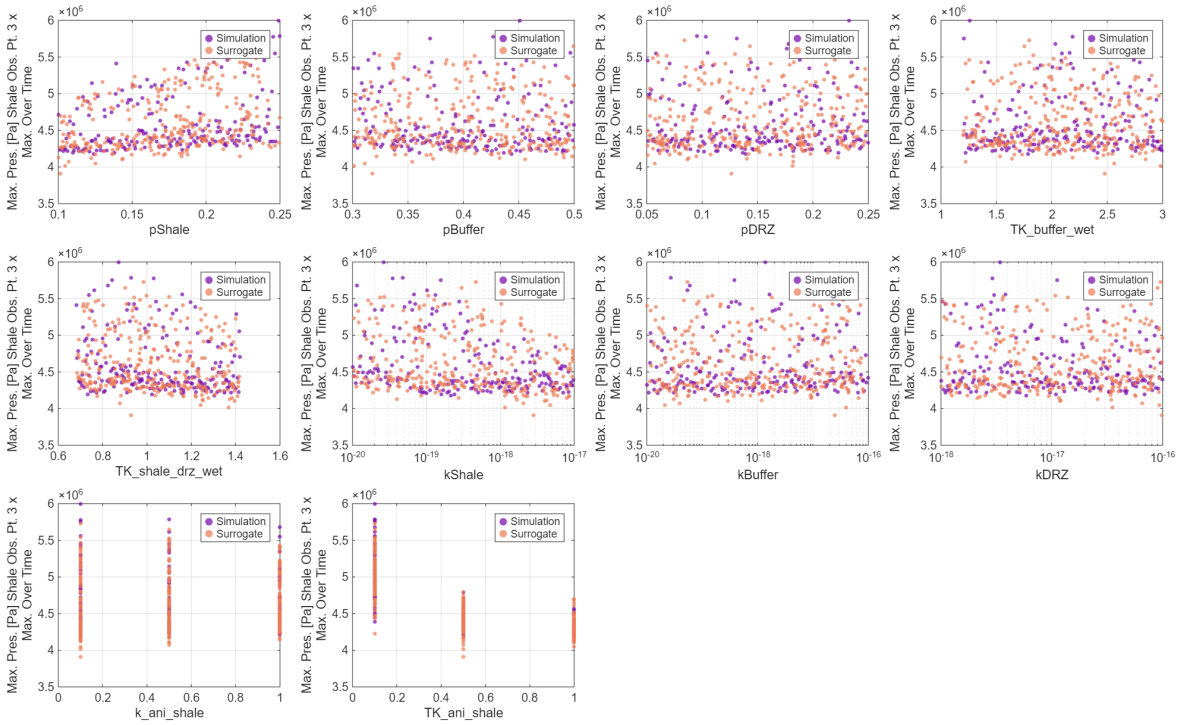

Figure 4-24 Scatterplots for the maximum pressure at shale observation point 3 in the x-direction

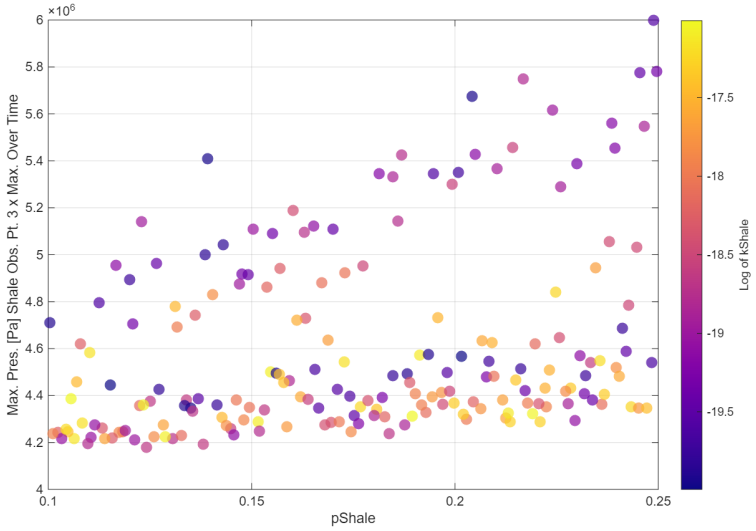

Figure 4-25 Scatterplot of the maximum pressure at shale observation point 3 in the x-direction versus pShale colored by kShale to show the interaction effect between shale porosity and permeability.

The time series plots for maximum pressure at the waste package observation point are shown in Figure 4-26. These plots show a more complex picture over time than the temperature plots. Early in the simulation, there appears to be an effect from kBuffer (top left) and TK_buffer_wet (top right). The effect of these parameters on the maximum pressure over time is less obvious: realizations with low permeability and low conductivity seem to experience maximum pressure earlier in the simulation time. This makes sense as low permeability in the buffer will lead to more pressure build up at the waste package and low conductivity in the buffer will cause temperature to build up, further increasing the pressure. There is also a clear effect late in the simulation from the shale thermal conductivity anisotropy ratio (bottom left), which is consistent with the Sobol' and scatterplot results. The shale permeability (bottom right) has a non-monotonic effect late in the simulation. Large shale permeability values are associated with earlier spikes in pressure at the waste package and the lowest shale permeability values are generally associated with later increases in pressure.

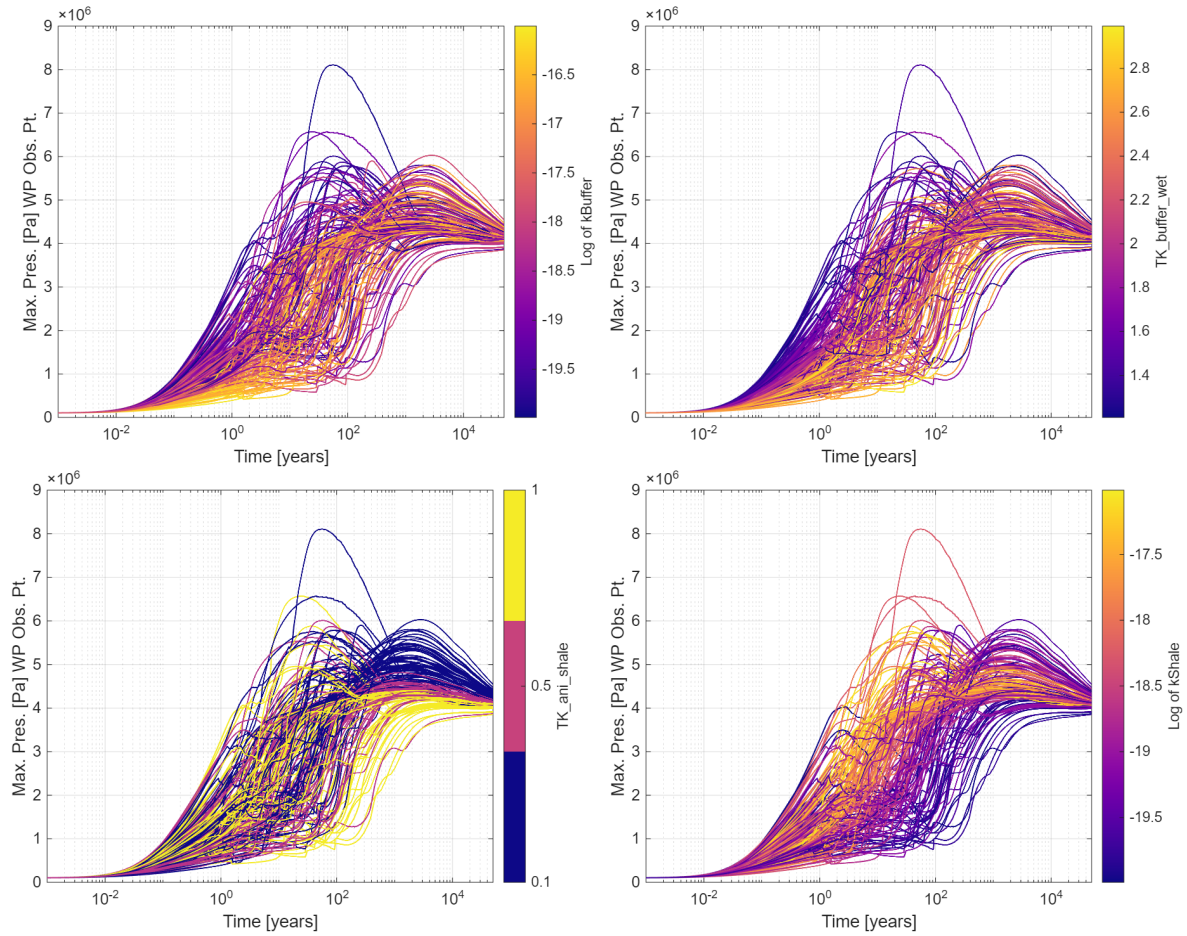

Figure 4-26 Time series plots of the maximum pressure at the waste package observation point colored by buffer permeability (top left), the buffer thermal conductivity (top right), shale thermal conductivity anisotropy ratio (bottom left), and shale permeability (bottom right)

The time series plots for the pressure at shale observation point 3 in the x-direction are shown in Figure 4-27 colored with respect to kshale (top left), TK_ani_shale (top right), and k_ani_shale (bottom left). The trend with kShale is distinctive with respect to timing. At high kShale values, the pressure decreases early at this observation point and gradually increases after around 10 years. For lower values of kShale, this pattern is somewhat delayed, and some realizations see an increase in pressure without a decrease. There is a clear effect from the shale thermal conductivity anisotropy ratio (top right) late in the simulation, which may interact with kShale late in the simulation. This would explain why the effect from kShale is less distinctive at the end of the simulation. The overall trend with respect to kShale, however, makes sense. Higher permeability should create less pressure build up. The shale permeability anisotropy ratio does not have a significant effect on the maximum pressure (thus why it was not significant in the Sobol' or scatterplot analysis). However, the time series plot shows that there is some effect on pressure. The lowest values of the anisotropy ratio (indicating higher horizontal permeability than vertical permeability within the shale) correspond to realizations that experience the lowest minimum pressures within these simulations, but also the greatest variability in pressure; some of the realizations with the highest pressure also have the lowest permeability anisotropy ratio. Though this is not a quantity of interest in our analysis like the maximum pressure, it is still helpful for analyzing the behavior of the model. This observation point is within the horizontal plane of waste package. Higher permeability in this plane will lead to more flow and lower pressures. This model behavior makes sense.

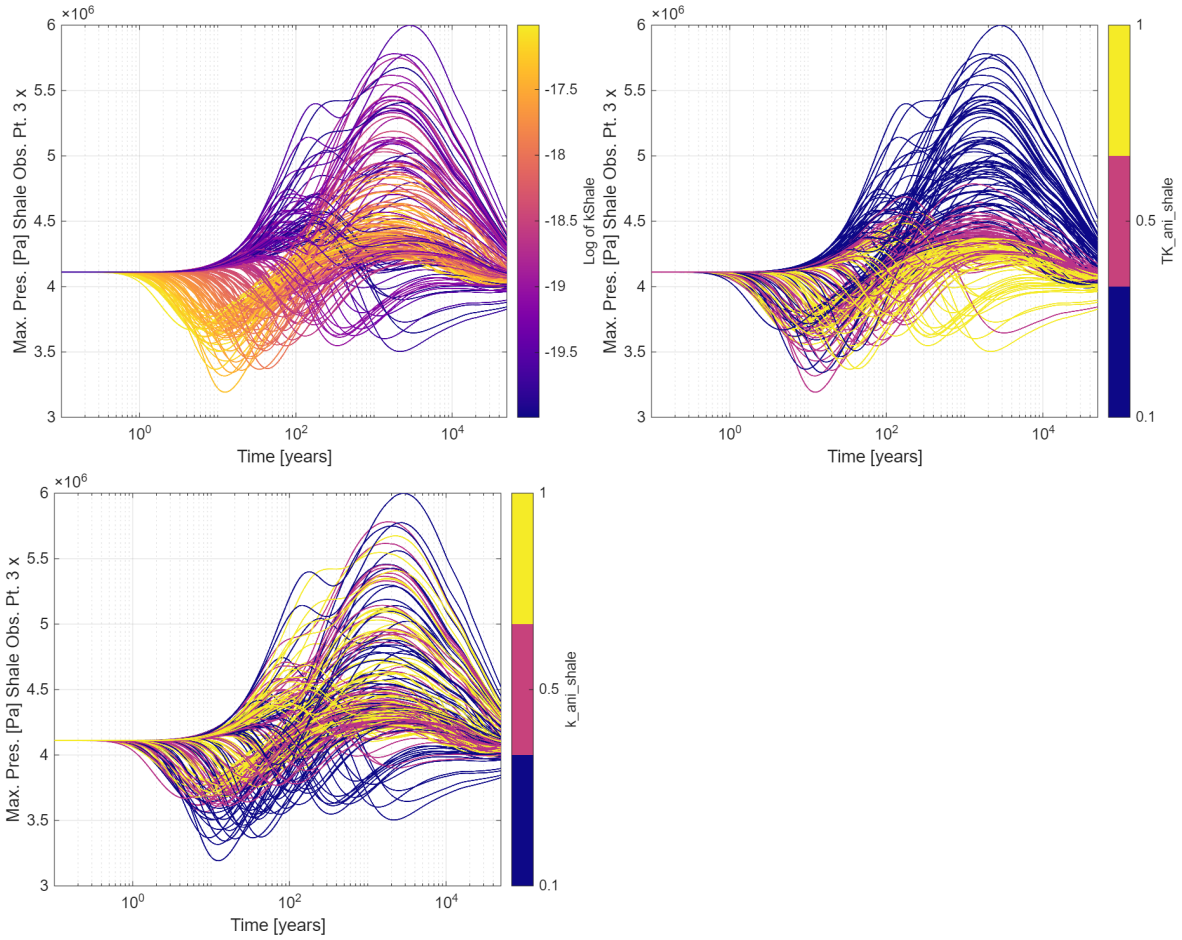

Figure 4-27 Time series plots of the maximum pressure at shale observation point 3 in the x-direction colored by shale permeability (top left), shale thermal conductivity anisotropy ratio (top right), and shale permeability anisotropy ratio (bottom).

The plots in Figure 4-28 plot the time of the maximum pressure versus the time of the maximum temperature at the waste package observation point (left) and shale observation point 3 in the x-direction (right). The dashed line indicates equal timing. We generated these plots to investigate the influence of temperature build up on pressure. At the waste package, the temperature peaks before pressure, which indicates that changes in temperature may drive pressure at this observation point. However, at observation points farther from the waste package, this is not always the case. The clustering of points at observation point 3 in the x-direction is caused by kShale and TK_ani_shale; kShale determines whether temperature peaks before pressure at this observation point and TK_ani_shale explains the horizontal clustering (difference in timing of maximum temperature).

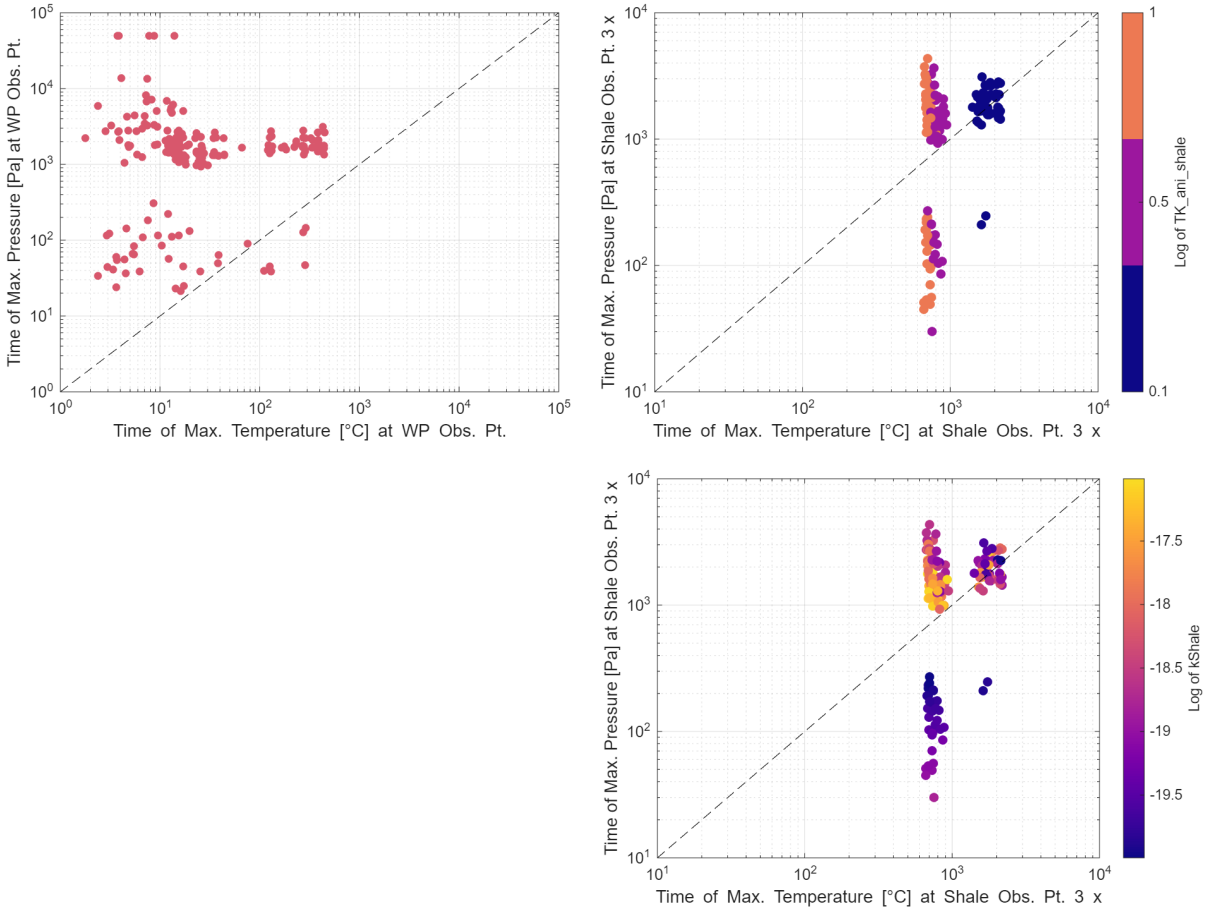

Figure 4-28 Scatter plots of the time of maximum pressure versus the time of maximum temperature as the waste package observation point (left) and shale observation point 3 in the x-direction (right and bottom).

The Sobol' index results for the maximum pressure at buffer observation point 2 in the y-direction are shown in Figure 4-29. Results for the first observation point in the buffer in the y-direction are not included here because the conclusions are the same for that observation point as for the waste package observation point. At observation point 2, the shale permeability is the dominant uncertainty, though there appear to be some interaction effects (some of which may be spurious since the total effects indices are present for all parameters). The scatterplots in Figure 4-30 indicate a strong relationship with kShale and a weaker relationship with kBuffer, which is consistent with the Sobol' indices for these parameters. The trend with respect to kBuffer appears only to occur at lower values of kBuffer, suggestive of an interaction effect. Another variable drives whether the maximum pressure is relatively high and, if so, there is a negative correlation with kBuffer for these higher-pressure realizations. The surrogate, however, seems to overestimate this trend. At high values of kBuffer, the surrogate predicts lower values of maximum pressure than seen in any of the simulations. The Sobol' index for kBuffer is likely an overestimate. More samples within the higher-pressure space could inform whether the relationship to kBuffer in that regime is due to chance or is a physical result. The interaction effect, however, is clearly between kShale and kBuffer. The scatter plot in Figure 4-31 shows the maximum pressure at this observation point plotted versus kBuffer colored by kShale. kShale determines whether the pressure is in the higher regime, and within this regime the pressure has a negative correlation to kBuffer.

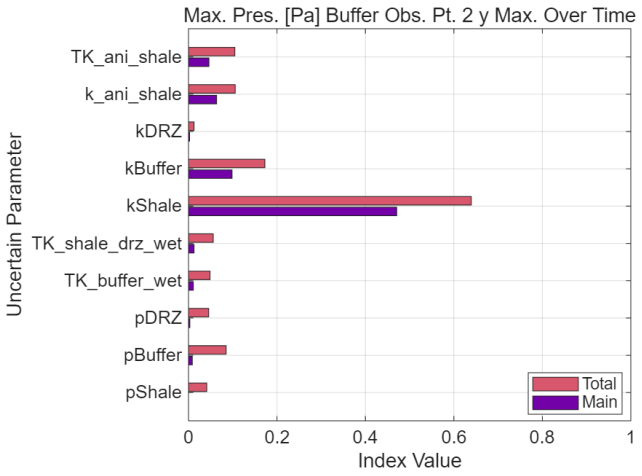

Figure 4-29 Maximum pressure Sobol' indices at buffer observation point 2 in the y-direction

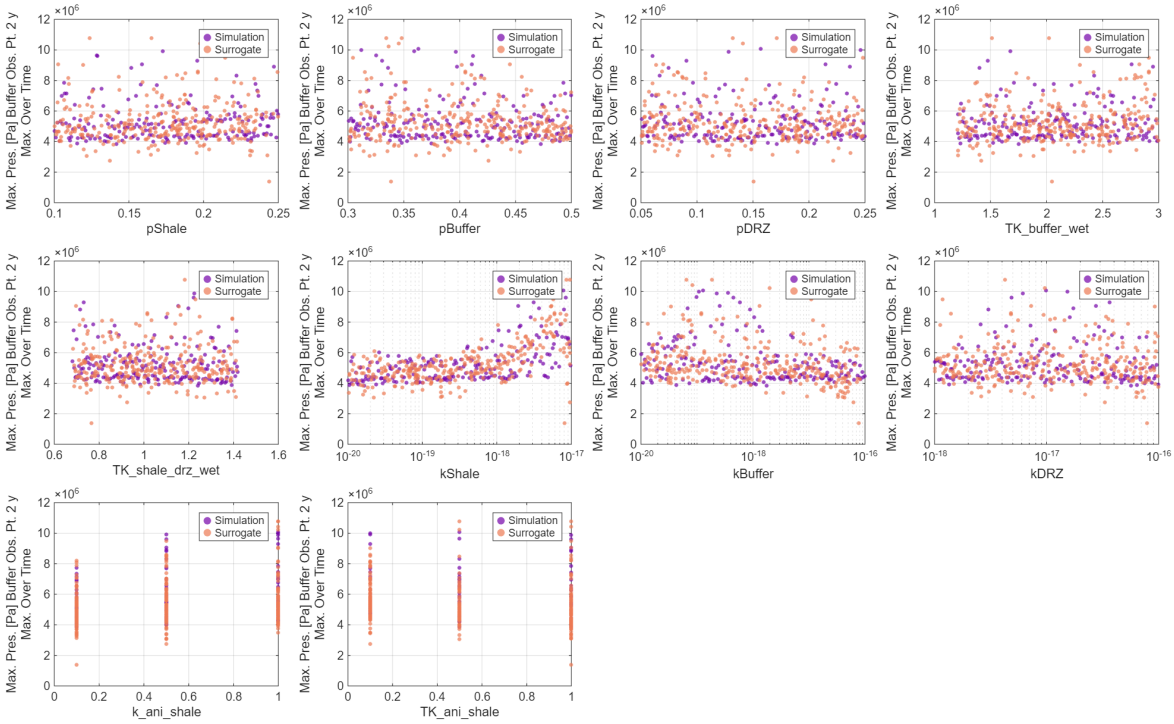

Figure 4-30 Scatterplots for the maximum pressure at buffer observation point 2 in the y-direction

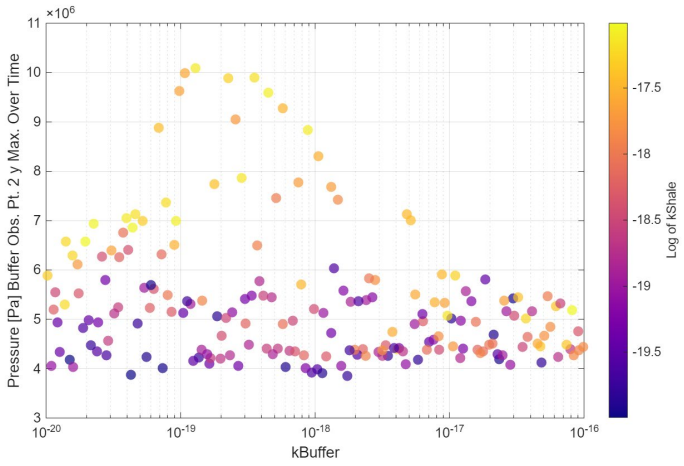

Figure 4-31 Interaction plot showing the combined effects of kBuffer and kShale on the maximum pressure at observation point 2 in the y-direction

Time series plots of the maximum pressure at this observation point are shown in Figure 4-32 colored by the shale thermal conductivity anisotropy ratio (top left), kShale (top right), and kBuffer (bottom). The shale permeability (kShale) affects the timing of pressure increases with higher permeability values leading to earlier increases in pressure. This is consistent with the behavior between shale permeability and pressure at the waste package and buffer observation points, though the effect is particularly strong at this observation point. The permeability of the buffer has a less monotonic effect. The peak pressures are associated with low buffer permeability, but some of the earliest realizations to see an increase in pressure have the highest values of kBuffer. This may be due to interaction effects between kShale and kBuffer.

The shale thermal conductivity anisotropy ratio has a similar effect at this observation point as it does at the waste package observation point. Around 100 years, low anisotropy ratios (high anisotropy) lead to higher pressures due to lower effective thermal conductivity and the highest anisotropy ratios (low anisotropy) lead to lower pressures due to higher effective thermal conductivity.

Sobol' index results for the maximum pressure at the lower sandstone observation point are shown in Figure 4-33. The shale thermal conductivity anisotropy ratio is clearly the dominant uncertainty on with some minor effect from the thermal conductivity of the shale and DRZ. Because the relationships between the input parameters and maximum pressure at this observation point are so clear, only the scatterplots for these two parameters are included in Figure 4-34; there are no significant input/output relationships in the other scatterplots. This is a clear interaction effect; the anisotropy ratio determines the relative magnitude of the maximum pressure; within that magnitude, the thermal conductivity of the shale and DRZ accounts for variation. At the lowest anisotropy ratio value (highest anisotropy), the thermal conductivity of the shale and DRZ has no effect; at a certain level, anisotropy dominates the thermal effect. This relationship is persistent across the whole time series, as shown in Figure 4-35.

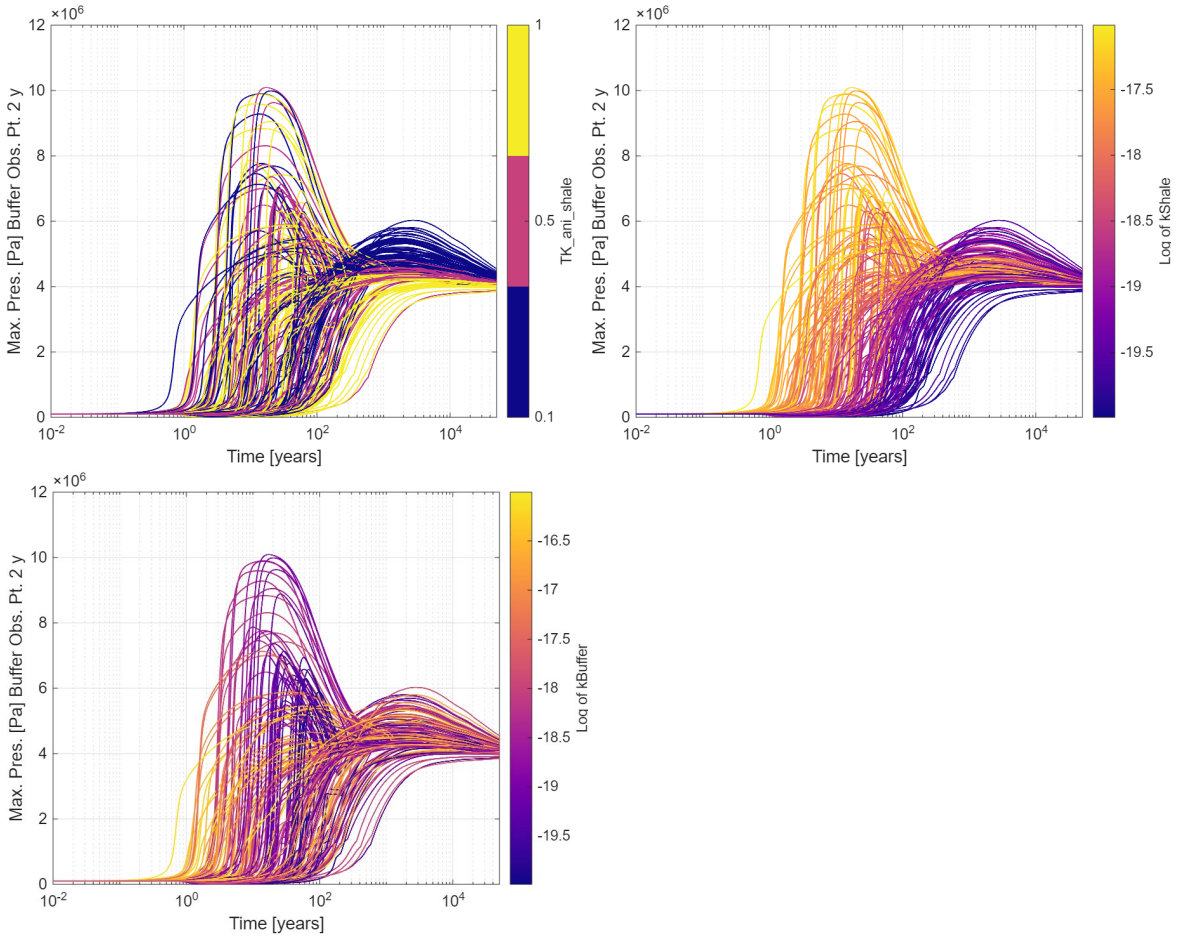

Figure 4-32 Time series plots of the maximum pressure at buffer observation point 2 in the y-direction colored by shale thermal conductivity anisotropy ratio (top left), shale permeability (top right), and buffer permeability (bottom)

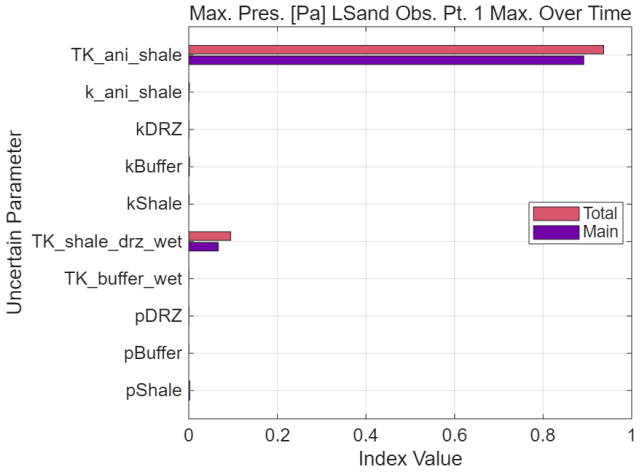

Figure 4-33 Maximum pressure Sobol' indices at lower sandstone observation point 1

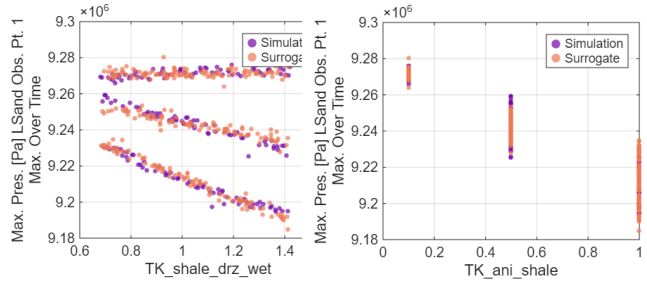

Figure 4-34 Scatterplots for the maximum pressure at lower sandstone observation point 1

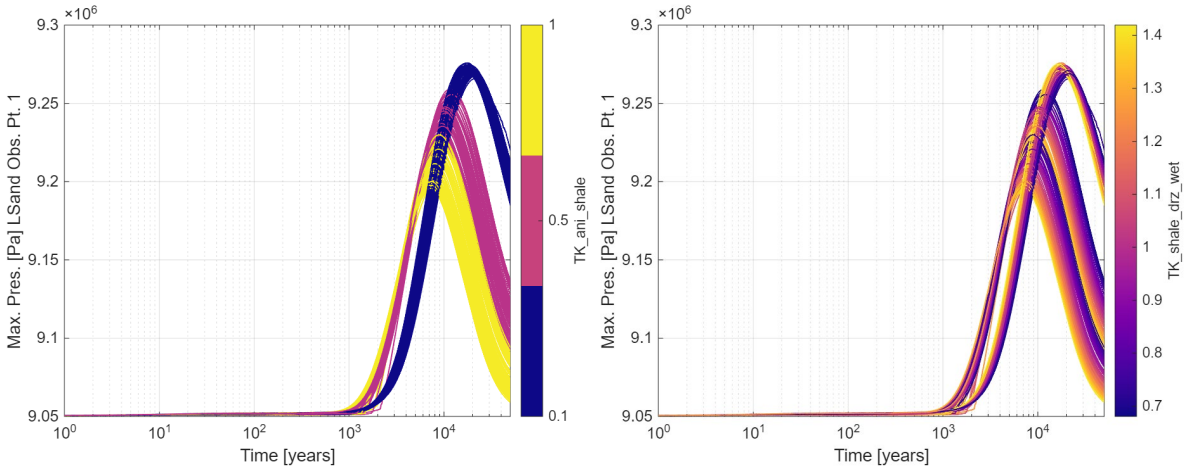

Figure 4-35 Time series plots of the maximum pressure at lower sandstone observation point 1 colored by shale thermal conductivity anisotropy ratio (left) and thermal conductivity of the shale and DRZ (right)

The Sobol' index results for the maximum pressure at limestone observation point 1 and shale observation point 4 are shown in Figure 4-36. The shale thermal conductivity anisotropy ratio continues to drive uncertainty at these observation points (and the point between them, which have similar results), however there are also effects from pShale, kShale, and TK_shale_drz_wet, which can all be observed is the scatterplots in Figure 4-37 and Figure 4-38. The shale porosity (pShale) has the clearest effect of these parameters, with a distinct positive linear trend. The trends with respect to the shale permeability (kShale) and the shale and DRZ thermal conductivity are both negative. The main difference between the limestone observation point and shale observation point 4 is that the shale thermal conductivity anisotropy ratio accounts for even more of the variance at the shale observation point than at the limestone observation point, having Sobol' index values approximately 0.1 greater in magnitude. Comparing the last plot frame between Figure 4-37 and Figure 4-38 confirms this Sobol' index result. Within the shale, the trend is stronger and the reduction in variance when the anisotropy ratio is 1 (low anisotropy) is more pronounced.

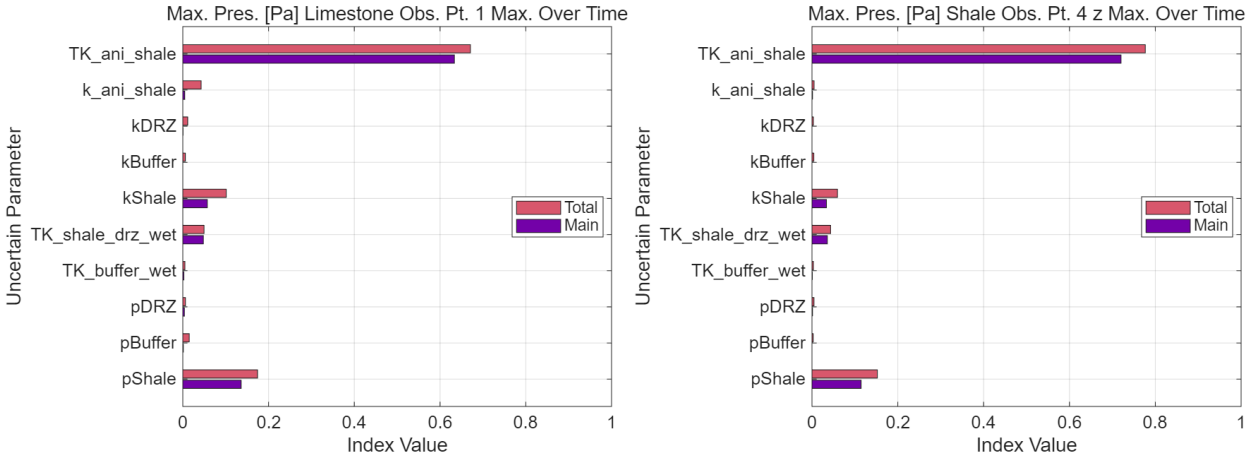

Figure 4-36 Maximum pressure Sobol' indices at limestone observation point 1 (left) and shale observation point 4 (right)

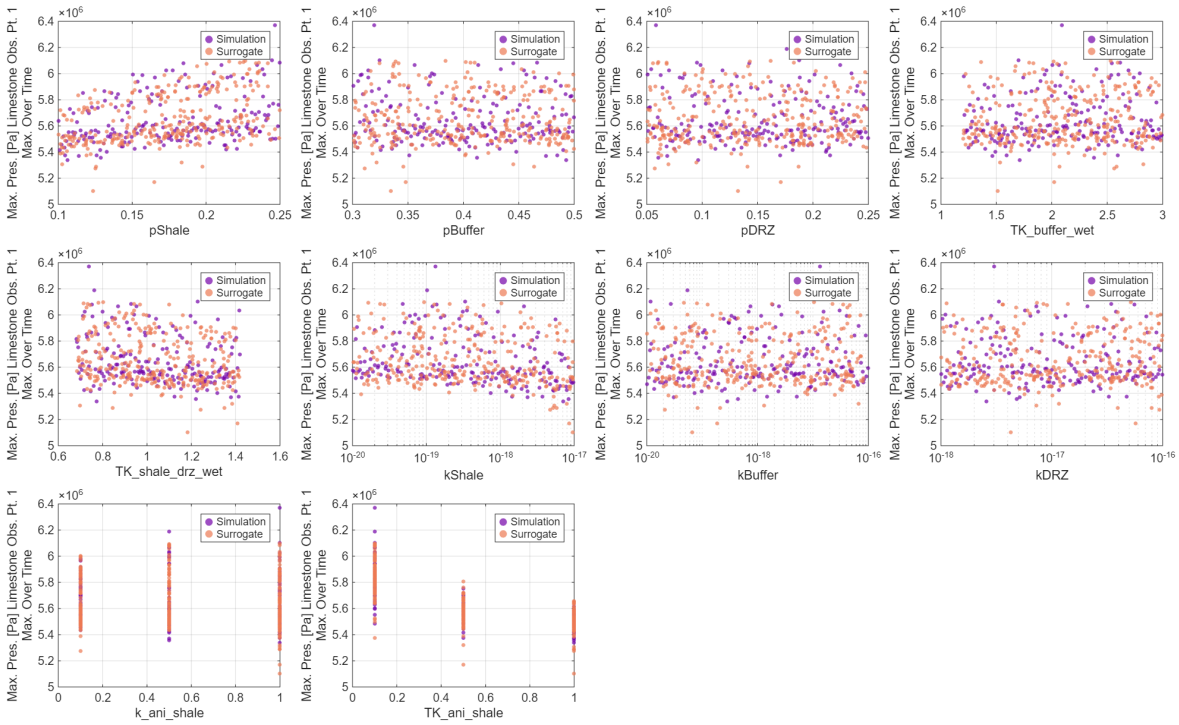

Figure 4-37 Scatterplots for the maximum pressure at limestone observation point 1

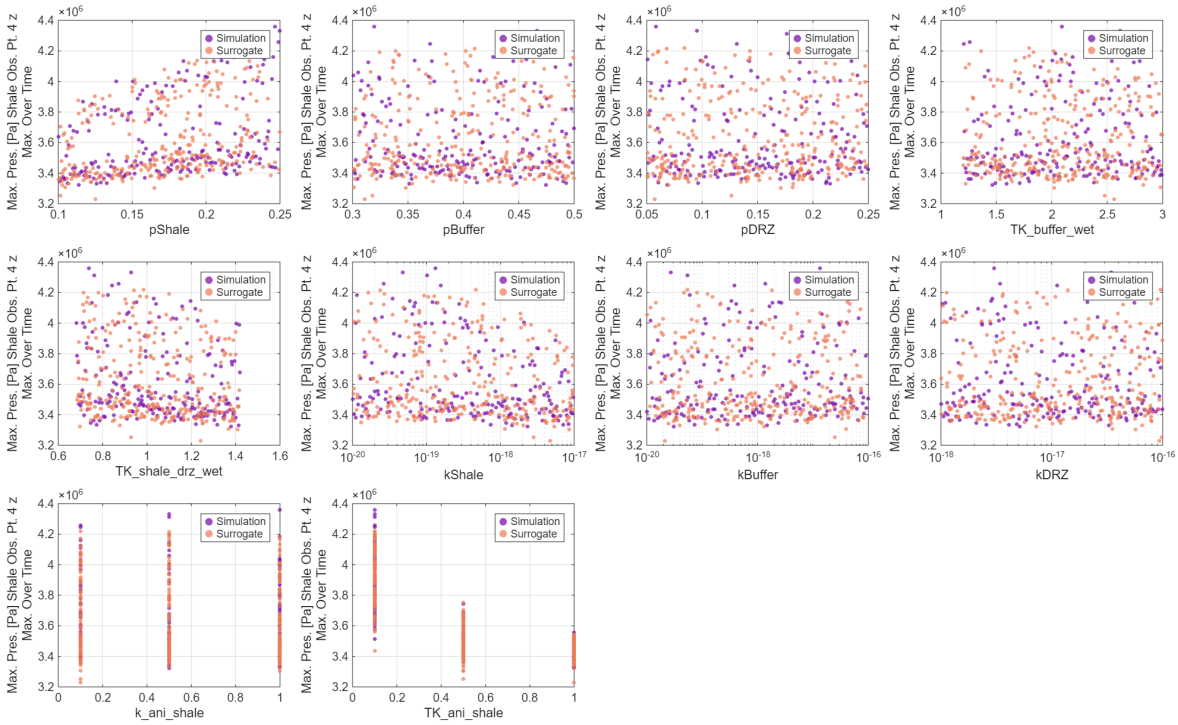

Figure 4-38 Scatterplots for the maximum pressure at shale observation point 4

The time series plots at limestone observation point 1 and sandstone observation point 4 give the same conclusions for the maximum pressure, so only the limestone plots are shown in Figure 4-39. High shale permeability is associated with earlier increases in maximum pressure and lower pressures later in the simulation (top left). High permeability will allow liquid to move into the shale, building pressure initially, but will also support movement through the shale, allowing the pressure to decrease over the course of the simulation. The relationship with low kShale values is less clear, but this appears to be an interaction effect with the shale thermal conductivity anisotropy ratio (top right). The realizations that have low shale permeability but see early increases in pressure also have a high thermal conductivity anisotropy ratio (low anisotropy), and hence higher effective thermal conductivity leading to an initial increase in pressure but lower peak. The realizations with low shale permeability that see an increase in pressure later also have the lowest thermal conductivity anisotropy ratio (most anisotropic), and less effective thermal conductivity. Pressure builds later, but peaks higher. The influences of pShale (shale porosity, bottom left) and TK_shale_drz_wet (shale and DRZ thermal conductivity, bottom right) are much less distinct. We see the effects on the peak that we see in the scatterplots, but trends over time are harder to discern because these variables are of secondary importance.

Finally, Sobol results for sandstone observation point 1 are shown in Figure 4-40. The significant total effect indices for almost all parameters with insignificant main effects for all but one parameter is suggestive of overfitting. The scatterplots in Figure 4-41 show a few important things. First, there is little variance in the maximum pressure at this topmost observation point. Second there are a handful of simulations with higher maximum pressure points than the rest of the simulations; these results are likely dominating the Sobol' index results. For kShale, these points are all clustered at the highest values of kShale.

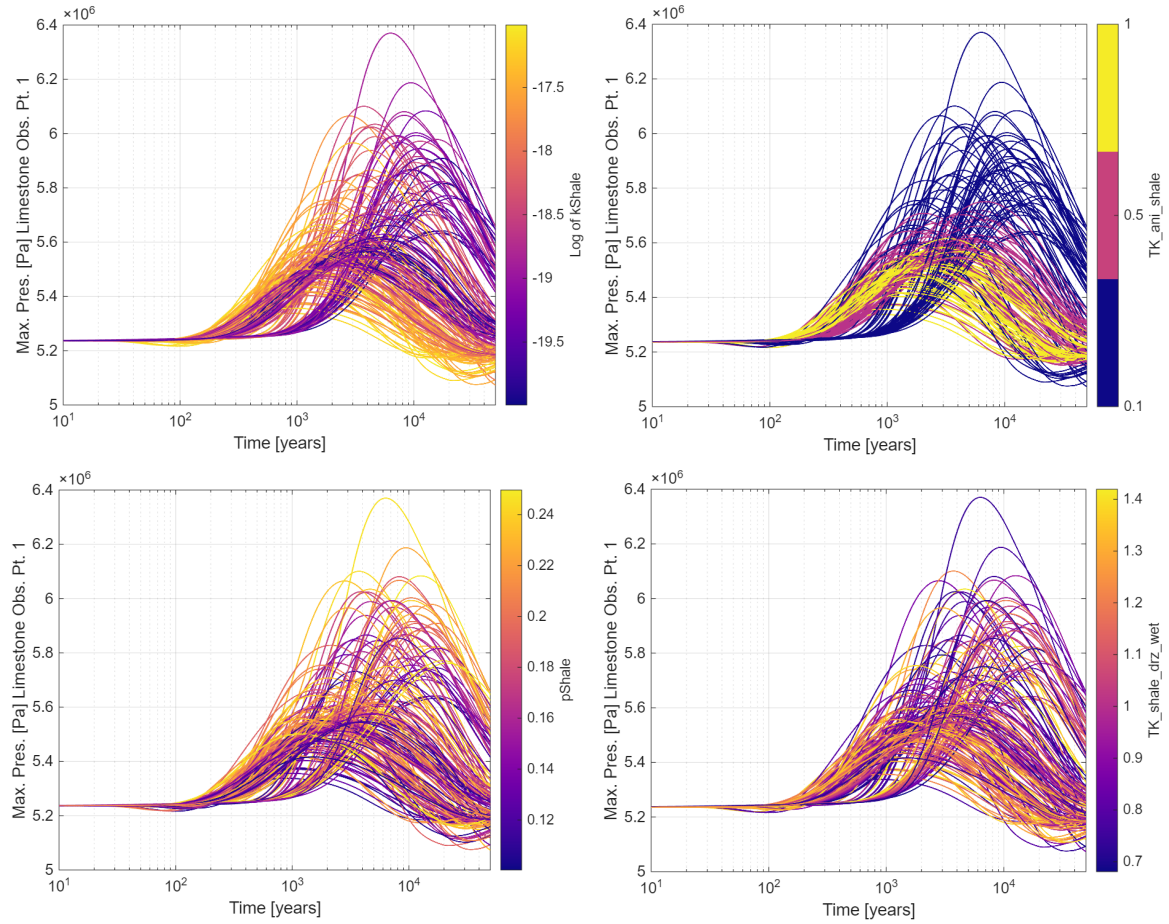

Figure 4-39 Time series plots of the maximum pressure at limestone observation point 1 colored by shale permeability (top left), shale thermal conductivity anisotropy ratio (top right), shale porosity (bottom left), and thermal conductivity of the shale and DRZ (bottom right)

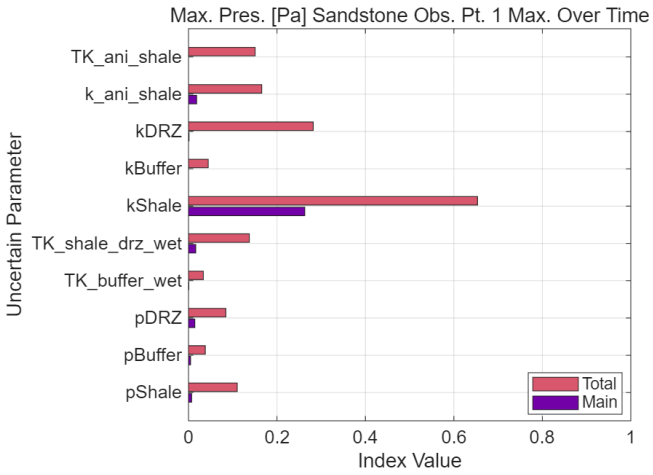

Figure 4-40 Maximum pressure Sobol' indices at sandstone observation point 1

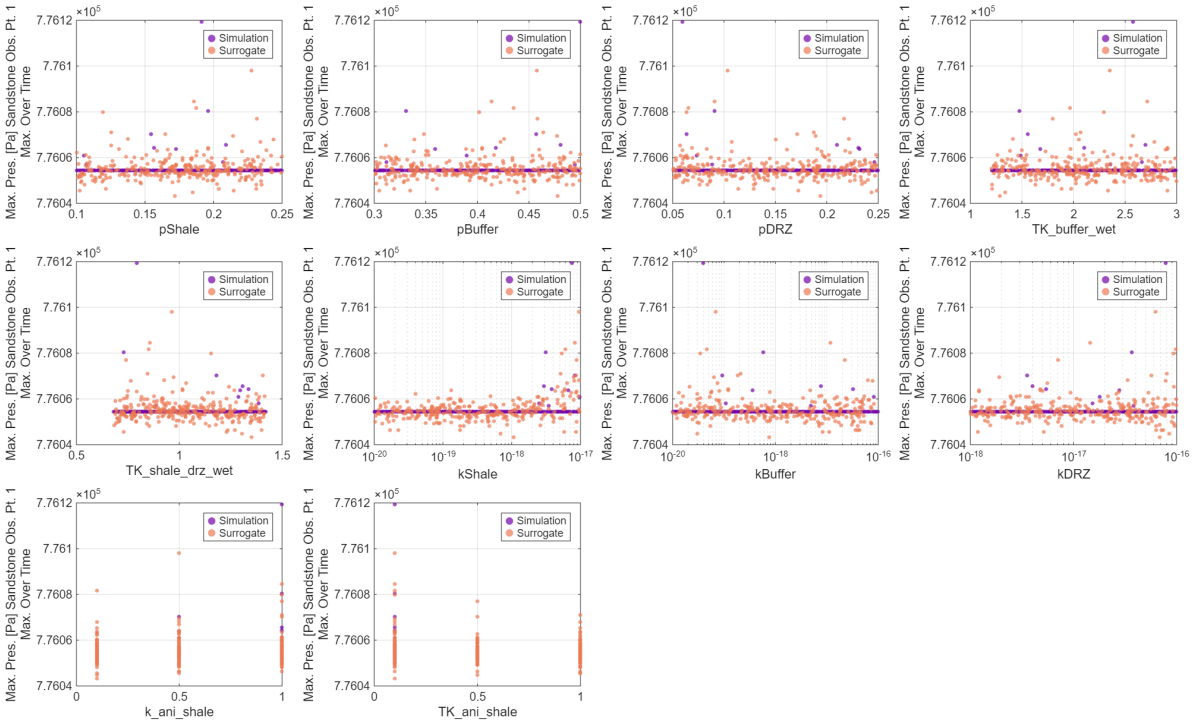

Figure 4-41 Scatterplots for the maximum pressure at sandstone observation point 1

The time series plots for maximum pressure at the sandstone observation point are shown in Figure 4-42 colored by the shale thermal conductivity anisotropy ratio (top left), shale and DRZ thermal conductivity (top right), and shale permeability (bottom left). The anisotropy ratio has a similar pronounced effect as at the other observation points. The interaction effect between the anisotropy ratio and the shale and DRZ thermal conductivity is interesting. The interaction effect is similar to what we saw at the lower sandstone observation point; TK_ani_shale determines the overall average magnitude and TK_shale_drz_wet determines variation around that average. However, at the sandstone observation point, that relationship does not always hold. There is also a significant effect from the shale permeability (bottom left). High permeability values are associated with the realizations that see an increase in pressure; these are the handful of realizations dominating the trend in the scatterplots.

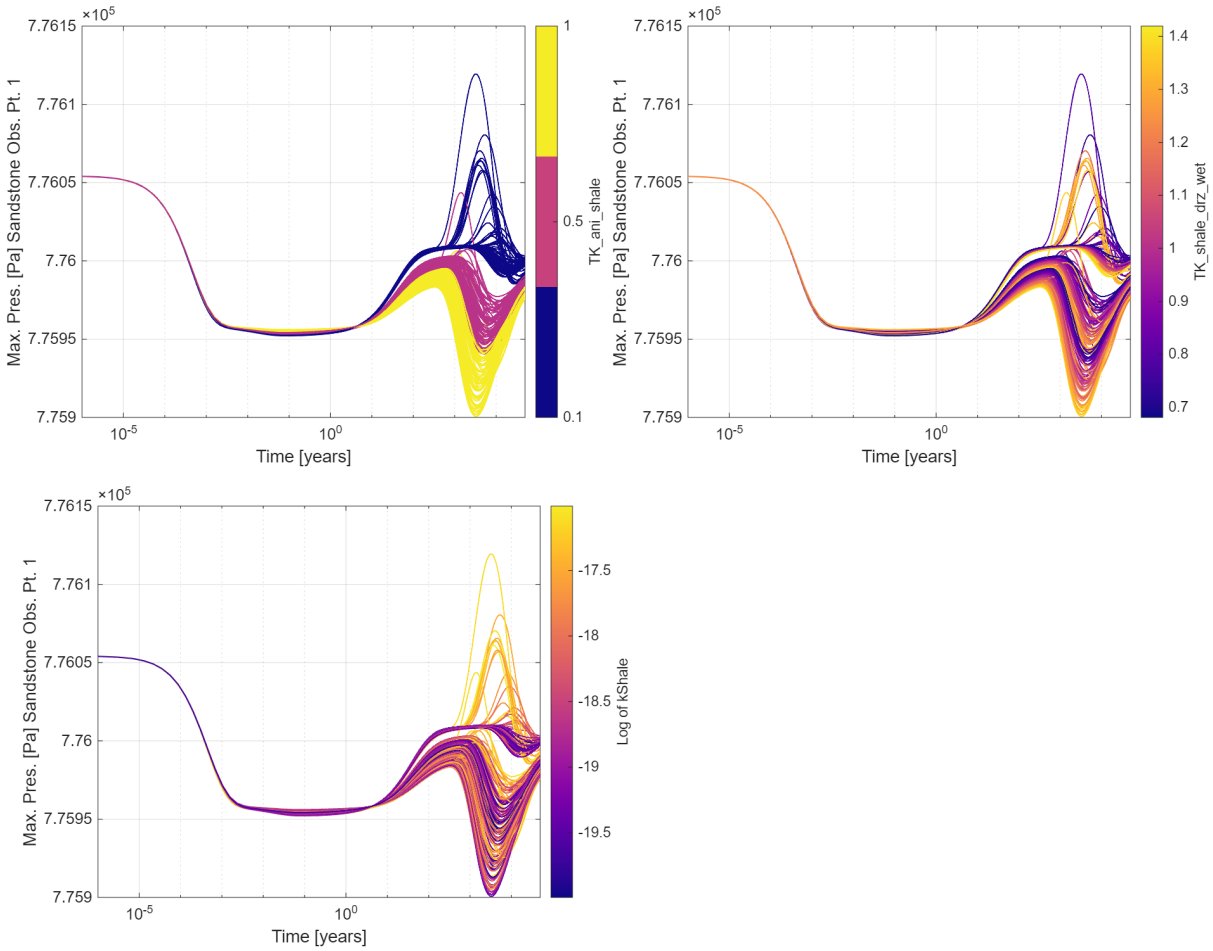

Figure 4-42 Time series plots of the maximum pressure at sandstone observation point 1 colored by the shale thermal conductivity anisotropy ratio (top left), shale/DRZ thermal conductivity (top right), and shale permeability (bottom)

4.3.3 LIQUID SATURATION

The liquid saturation always peaks at 1.0, so we do not have a scalar liquid saturation quantity of interest. Instead, we have time series plots of the liquid saturation colored by the different input parameter to qualitatively analyze the effects of input uncertainty on liquid saturation.

The liquid saturation over time at the waste package observation point is shown in Figure 4-43 colored by the buffer thermal conductivity (top left), buffer permeability (top right), and shale permeability (bottom). The buffer parameters both appear to have an effect early. Low thermal conductivity and high permeability are associated with the earliest reductions in liquid saturation. This effect of low thermal conductivity may be due to increasing temperature creating a gas phase. Thermal conductivity also drives pressure early in the simulation at this observation point, which can increase gas or liquid flow into and through the buffer. The buffer permeability has more of an effect than the buffer thermal conductivity on the subsequent increase in liquid saturation. Both the buffer and shale permeabilities are negatively correlated with the timing of liquid saturation increase; higher permeabilities lead to earlier increases in liquid saturation.

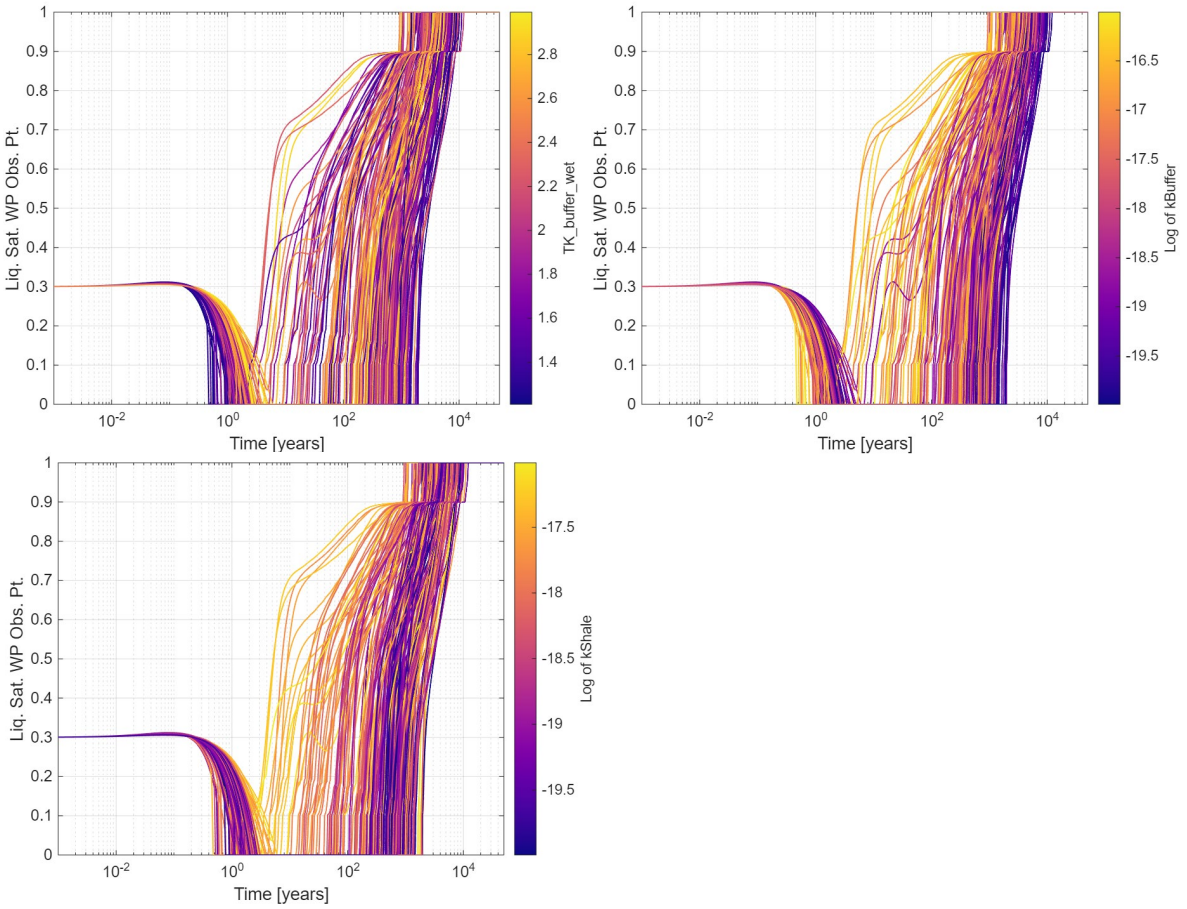

Figure 4-43 Time series plots of the liquid saturation at the waste package observation point colored by the buffer thermal conductivity (top left), buffer permeability (top right), and shale permeability (bottom)

At buffer observation point 1 in the x-direction, the two parameters that appear to drive liquid saturation are the buffer permeability (Figure 4-44, left) and the shale permeability (Figure 4-44, right). The buffer permeability has the early effect, with higher permeabilities leading to earlier saturation at the buffer observation point. A more permeable buffer will allow fluid to flow into the buffer, saturating the material at this observation point earlier in the simulation. Low permeability in the shale is associated with realizations that see a subsequent decrease in liquid saturation, with some realizations seeing dry out at this observation point.

The liquid saturation at buffer observation point 2 in the x-direction is not plotted because the sensitivity analysis conclusions are the same. However, note that the liquid saturation at observation point 2 in the buffer does not decrease to zero as it does at observation point 1. There are no realizations for which dry out occurs at observation point 2 in the buffer.

The time series plot of the liquid saturation at DRZ observation point 2 in the x-direction is shown in Figure 4-45 colored by the shale permeability (left) and the DRZ permeability (right). The liquid saturation is strongly dominated by the shale permeability but there is some effect from the DRZ permeability. This far from the waste package, there is no more effect from thermal conductivity; the liquid saturation is driven by permeabilities. We note also that the shale permeability parameter varies more than the DRZ permeability and there is more shale than DRZ in the model.

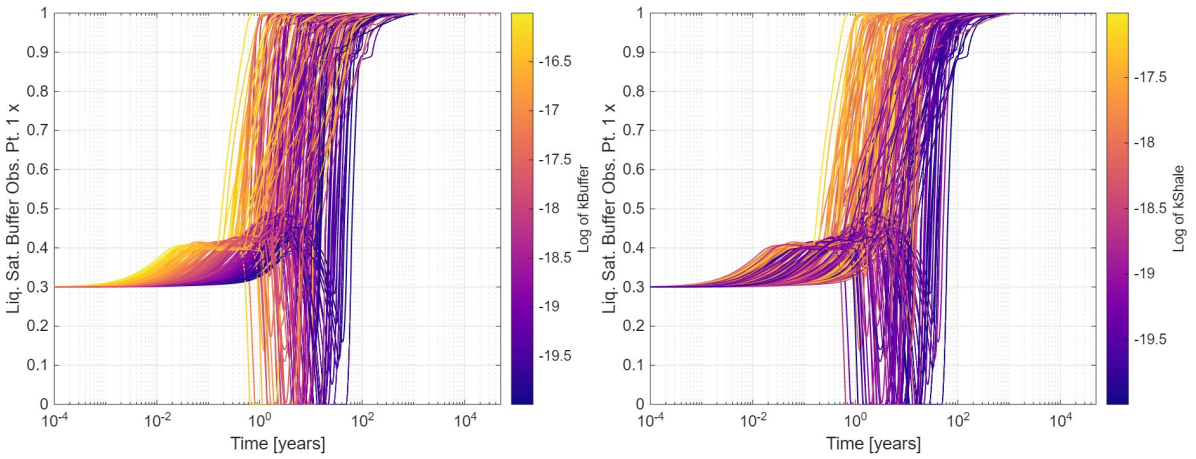

Figure 4-44 Time series plots of the liquid saturation at buffer observation point 1 in the x direction colored by the buffer permeability (left) and the shale permeability (right)

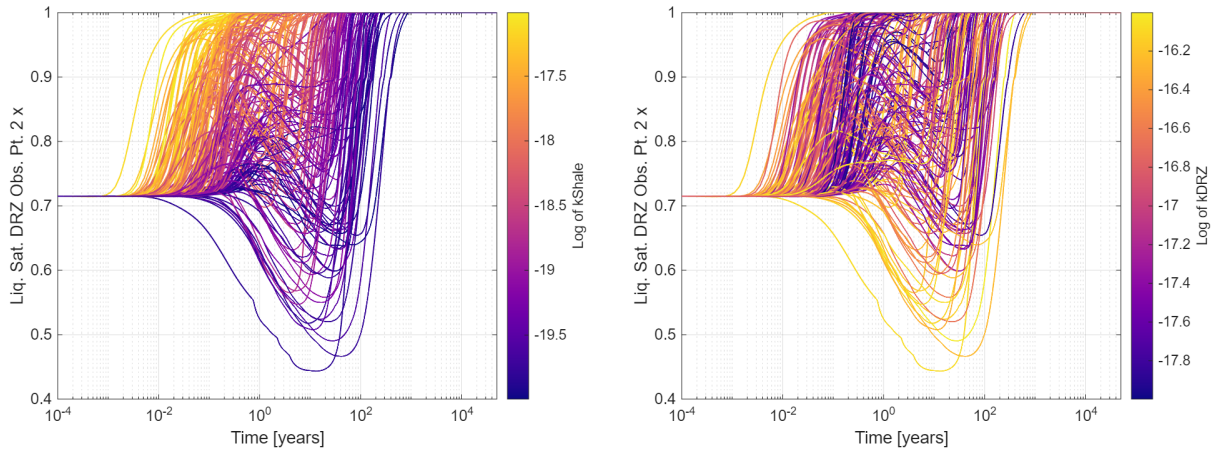

Figure 4-45 Time series plot of the liquid saturation at DRZ observation point 2 in the x-direction colored by the shale permeability (left) and the DRZ permeability (right)

4.3.4 SENSITIVITY ANALYSIS SUMMARY

Overall, the shale thermal conductivity anisotropy ratio was a driving uncertainty on maximum pressure and temperature at many observation points. Temperatures were affected by uncertainty in this anisotropy ratio as well as other uncertain thermal conductivity parameters, but not by parameters associated with other physical processes (e.g., permeabilities, porosities). Though temperatures affected pressure, especially near the waste package, the SA results for pressure were more varied and appear to reflect the complex interaction of multiple physical processes. The shale thermal conductivity anisotropy ratio was also a dominant uncertainty for pressure, but had significant interaction effects with thermal conductivity parameters, permeabilities, and porosities, depending on the observation point. Variation in liquid saturation at all observation points was dominated by permeability parameters, but the more interesting result for liquid saturation was the lack of complete dry out in the buffer region. Some realizations experienced dry out at observation point 1 in the x-direction and y-directions in the buffer, but none of the realizations experienced dry out at observation point 2 in these directions.

5 INTERNATIONAL ENGAGEMENTS

In addition to the work outlined in Chapters 2-5, the UQ/SA team participated in JOSA and DECOVALEX this year. These activities are described in sections 5.1 and 5.2, respectively.

5.1 JOSA VOLUME 2 REPORT

Laura Swiler and Dusty Brooks continued their involvement in the Joint Sensitivity Analysis (JOSA) international working group. Laura co-leads this group with Klaus Röhlig and Dirk Becker from Germany. This group held a series of virtual meetings over the past year on the following dates: August 21, September 25, November 20 (in 2024) and January 15, February 26, May 7, June 18, and July 31 (in 2025). The purpose of these meetings is to demonstrate and apply the latest state-of-the art sensitivity analysis methods to realistic case studies provided by the participating organizations. These organizations include GRS and TU-Clausthal in Germany, POSIVA in Finland, SCK-CEN in Belgium, and Enresa in Spain.

This year, we completed and published Volume 2 of the JOSA case studies (Swiler L. P., et al., 2025):

> Laura P. Swiler, Dirk-Alexander Becker, Dusty Brooks, Lasse Koskinen, Pekka Kupiainen, Elmar Plischke, Klaus-Jürgen Röhlig, Javier Samper, Sabine M. Spiessl. "Sensitivity Analysis Comparisons on Geologic Case Studies: An International Collaboration, Volume 2" SAND2025-00230.

Volume 2 had three case studies: a Low- and Intermediate-Level Waste (LILW) repository installed in an abandoned former salt production mine from the GRS team, a generic crystalline reference case for High Level Waste (HLW) with varying discrete fracture networks as well as epistemic parameters provided by Sandia, and a reactive transport case involving HLW provided by Enresa. The culmination of the Volume 2 report was the final chapter which summarized best practices and recommendations for a practitioner employing sensitivity analyses to real application studies. These best practices are now being prepared for a journal article.

The JOSA team has started a new set of case studies which will be the basis for Volume 3. The first of these case studies is a geochemical model developed by SCK-CEN. The model was developed in the PHREEQC code to simulate the sorption of Americium on organic matter-containing Boom Clay. The model incorporates cation exchange and surface complexation on clay minerals, along with sorption on organic substances. It employs the Tipping model, a widely used mathematical framework for describing metal sorption on organic acids. Simulations were conducted across a range of initial Americium concentrations, producing a sorption isotherm ($\log(K_d)$) as a function of Am-concentration. The model requires 50 inputs, and SCK-CEN provided the JOSA team with one million simulation runs (a table with one million samples of 50 inputs and $\log(K_d)$ output values). This case study has been very interesting for JOSA and SNL to consider as it pushes the boundaries of scaling our sensitivity analysis methods: we have not tackled a problem with 1M samples in 50 input dimensions previously. Our preliminary findings are that we need to be cautious when utilizing surrogate models in such high-dimensional problems as they may mis-represent or under-represent the actual variance, as we demonstrated with the PCE method which underrepresented the variance and thus over-estimated the Sobol' sensitivity indices.

We plan to continue investigation of this geochemistry case study as well as other case studies that will be investigated by the JOSA participants for Volume 3 in the coming year.

5.2 DECOVALEX

The DECOVALEX (DEvelopment of COupled Models and their VAlidation against EXperiments) is a large, multi-year, multi-organization international project focused on thermal-hydraulic-mechanical-chemical processes and their influence on repository performance and safety. In the last four-year DECOVALEX project (DECOVALEX-2023), Sandia participated in tasks related to generic salt and crystalline reference case model development and analyses.

For the current four-year DECOVALEX project (running from 2024-2027, referred to as DECOVALEX-2027), Sandia serves as the task lead for the crystalline portion of Task F, which involves crystalline generic reference case modeling. In DECOVALEX-2027, a primary focus for Task F is on uncertainty quantification and sensitivity analysis. Members of the GDSA UQ/SA team have supported the initial Task F specification for DECOVALEX-2027 and are participating in this exercise. UQ studies on a simple benchmark problem have been completed, and the sampling procedure for a larger, realistic uncertainty analysis on the full DECOVALEX crystalline reference case has been defined (contact the authors for the initial Task specification). The UQ/SA studies focus on a nested sampling plan with outer loop sampling of discrete fracture networks and inner loop sampling of epistemic parameters including waste package properties and backfill and buffer permeabilities and porosities. These studies will be run by participating organizations during the next year of DECOVALEX-2027.

6 SUMMARY

This report described activities performed in fiscal year 2025 associated with the GDSA Uncertainty and Sensitivity Analysis Methods work package, as summarized below.

The GDSA UQ/SA team worked closely with the GDSA Biosphere model development team at PNNL to perform sensitivity analysis for the Biosphere model (see Chapter 2). Dakota was integrated in a coupled sensitivity analysis, where Dakota first ran a PFLOTRAN model which generated radionuclide concentrations that were input to the Biosphere model. Parameters of both the PFLOTRAN and the Biosphere model were sampled, and a SA study was performed to identify the dominant parameters contributing to total effective dose. The study paves the way for larger coupled PFLOTRAN-Biosphere model analyses.

This year, we summarized various approaches to characterizing the effects of spatial heterogeneity with proxy variables in a SAND report. This report outlines progress to date and remaining challenges.

A main focus of our work package this year was sensitivity analysis for a quarter WP shale case with increased resolution in the modeling domain near the waste package. The quantities of interest were the liquid saturation, temperature, and maximum pressure at observation points at the waste package, and in the buffer, DRZ, shale, lower sandstone, limestone, silt, and sandstone. The majority of the observation points were in the near-field because the study focused on understanding conditions in which the repository might get too hot with pressures that are too high. Sensitivity analysis was performed using Sobol' indices estimated with polynomial chaos expansion, scatterplots, and time series plots colored by uncertain input parameters. We found that the shale thermal conductivity anisotropy ratio was the dominant uncertainty driving maximum temperature variability; there are also significant effects from the other thermal conductivity parameters, but no parameter related to other physical processes. The shale thermal conductivity anisotropy ratio was also a prominent driving uncertainty on the maximum pressure, however, there were interaction effects between this ratio and either thermal conductivity or permeability and porosity parameters depending on the observation point. Liquid saturation was affected by thermal conductivity at the waste package, but elsewhere it is driven by the uncertain permeabilities. We found that dry out did not occur for any realizations at observation point 2 in the buffer and only for some realizations at observation point 1 in the buffer. The entire buffer region does not dry out.

In terms of our international engagements, we are supporting the next four-year phase of DECOVALEX which has an emphasis on UQ/SA for the crystalline reference case. We continue to work with the Joint Sensitivity Analysis Working Group: we issued the Volume 2 SAND report summarizing the result of various SA studies on the case studies provided by the participating organizations and are now working on Volume 3 with new case studies.

7 REFERENCES

Adams, B., Bohnhoff, W., Dalbey, K., Ebeida, M., Eddy, J., Eldred, M., . . . Winokur, J. (2022). *Dakota, A Multilevel Parallel Object-Oriented Framework for Design Optimization, Parameter Estimation, Uncertainty Quantification, and Sensitivity Analysis: Version 6.16 User's Manual.* Albuquerque, New Mexico: SAND2022-6171, Sandia National Laboratories.

Basurto, E., LaForce, T., Swiler, L. P., Brooks, D. M., Leone, R., & Mariner, P. E. (2025). *Near Repository Investigations for Disposal of Hot SNF in an Argillite Repository.* Albuquerque, NM: Sandia National Laboratories.

Brooks, D., Swiler, L., Stein, E., Mariner, P., Basurto, E., Portone, T., . . . Leone, R. (2022). Sensitivity analysis of generic deep geologic repository with focus on spatial heterogeneity induced by stochastic fracture network generation. *Advances in Water Resources, 169*, 104310. doi:doi.org/10.1016/j.advwatres.2022.104310.

Ghosh, S., Snyder, S. F., Hargraves, J., Condon, C., Hammon, G., & Napier, B. A. (2023). *GDSA Biosphere Model Design Document.* Pacific Northwest National Laboratory, PNNL-32062 – Rev. 3.

Hammond, G., Lichtner, P., & Mills, R. (2014, http://doi.org/10.1002/2012wr013483). Evaluating the performance of parallel subsurface simulators: Ann illustrative example with PFLOTRAN. *Water Resources Research, 501*(1), 208-228. doi:10.1002/2012wr013483

Hammond, G., Lichtner, P., Mills, R., & Lu, C. (2008). Toward petascale computing in geosciences: application to the Hanford 300 Area. (R. Stevens, Ed.) *Journal of Physics: Conference Series, SciDAC 2008: Scientific Discovery through Advanced Computing, 125*(012051).

Helton, J., & Marietta (Editors), M. (2000). Special Issue: The 1996 Performance Assessment for the Waste Isolation Pilot Plant. *Reliability Engineering and System Safety*(69), 1-451.

Helton, J., Hansen, C., & Swift (Editors), P. (2014). Special Issue: Performance Assessment for the Proposed High-Level Radioactive Waste Repository at Yucca Mountain, Nevada. *Reliability Engineering and System Safety, 122*, 1-456.

Islas Quinones, E., & Portone, T. (2024). Computationally Efficient Computation of Sobol' Main Effects Indices for Discrete Random Variables. *(In Preparation)*.

LaForce, T., Basurto, E., Bigler, L., Chang, K. W., Good, F., Hasiuk, F., . . . Mariner, P. (2024). *GDSA Repository Systems Analysis Investigations in FY2024.* Albuquerque, New Mexico: Sandia National Laboratories, M2SF-24SN010304092.

LaForce, T., Basurto, E., Bigler, L., Chang, K., Ebeida, M., Jayne, R., . . . Sharpe, J. (2023). *GDSA Repository Systems Analysis Investigations in FY2023.*

Li, C., & Mahadevan, S. (2016). An Efficient Modularized Sample-Based Method to Estimate the First-Order Sobol' Index. *Reliability Engineering & System Safety, 153*, 110-121. doi:10.1016/j.ress.2016.04.012

Lichtner, P., & Hammond, G. (2012). *Quick Reference Guide: PFLOTRAN 2.0 (LA-CC-09-047) Multiphase-Multicomponent-Multiscale Massively Parallel Reactive Transport Code.* Los Alamos, New Mexico: LA-UR-06-7048. Los Alamos National Laboratory.

Mariner, P., Basurto, E., Brooks, D., Curry, C., Debusschere, B., Fukuyama, D., . . . Swiler, L. (2024). *GDSA Framework Development and Process Model Integration FY2024.* Sandia National Laboratories, Albuquerque NM.

Mariner, P., Gardner, W., Hammond, G., Sevougian, S., & Stein, E. (2015). *Application of Generic Disposal System Models.* Albuquerque, New Mexico: FCRD-UFD-2015-000126; SAND2015-10037R. Sandia National Laboratories.

Mariner, P., Stein, E., Frederick, J., Sevougian, S., & Hammond, G. (2017). *Advances in Geologic Disposal System Modeling and Shale Reference Cases.* Albuquerque, New Mexico: SFWST-2017-000044; SAND2017-10304R. Sandia National Laboratories.

Mariner, P., Stein, E., Frederick, J., Sevougian, S., Hammond, G., & Fascitelli, D. (2016). *Advances in Geologic Disposal System Modeling and Application to Crystalline Rock.* Albuquerque, New Mexico: FCRD-UFD-2016-000440; SAND2016-9610R. Sandia National Laboratories.

Mariner, P., Stein, E., Sevougian, S., Cunningham, L., Frederick, J., Hammond, G., . . . Basurto, E. (2018). *Advances in Geologic Disposal Safety Assessment and an Unsaturated Alluvium Reference Case.* Albuquerque, New Mexico: SFWST-2018-000509; SAND2018-11858R. Sandia National Laboratories.

Napier, B. A., Strenge, D. L., Ramsdell, J. V., Eslinger, P. W., & Fosmire, C. J. (2004). *GENII Version 2 Software Design Document.* doi:10.2172/981612

Park, H., Fukuyama, D., Leone, R., Madsen, C., Paul, M., Salazar, A., & Rechard, R. (2024). *2024 Advancements in PFLOTRAN Development for GDSA Framework.* Sandia National Laboratories, Albuquerque NM.

Portone, T., Eckert, A., Basurto, E., Friedman-Hill, E., & Swiler, L. (2024). GDSA framework, a computational framework for complex modeling problems in radioactive waste management. *Nuclear Engineering and Technology*. doi:https://doi.org/10.1016/j.net.2024.06.008

Portone, T., Eckert, A., Basurto, E., Friedman-Hill, E., & Swiler, L. (submittal). A Graphical Workflow Supporting Complex Modeling Problems. *Journal of High Performance Computing*.

Prieur, C., & Tarantola, S. (2017). Variance-Based Sensitivity Analysis: Theory and Estimation Algorithms. In R. G. al. (Ed.), *Handbook of Uncertainty Quantification* (pp. 1217-1239). Springer International Publishing. doi:10.1007/978-3-319-12385-1_35.

Saltelli, A., Annoni, P., Azzini, I., Campolongo, F., Ratto, M., & Tarantola, S. (2010). Variance Based Sensitivity Analysis of Model Output. Design and Estimator for the Total Sensitivity Index. *Computer Physics Communications, 181*(2), 259-270. doi:10.1016/j.cpc.2009.09.018

Sevougian, S., Hammond, G., Mariner, P., Stein, E. F., & MacKinnon, R. (October 10-11, 2018). GDSA Framework: High Performance Safety Assessment Software to Support the Safety Case. *Proceedings of the IGSC Safety Case Symposium, 2018.* Rotterdam, The Netherlands,: SAND2018-9975C, Sandia National Laboratories. Albuquerque, New Mexico.

Sobol', I. (2001, http://doi.org/10.1016/S0378-4754(00)00270-6). Global sensitivity indices for nonlinear mathematical models and their Monte Carlo estimates. *Mathematics and Computers in Simulation, 55*(1-3), 271-280. doi:10.1016/S0378-4754(00)00270-6

Staven, L. H., Napier, B. A., Rhoads, K., & Strenge, D. L. (2003). *A Compendium of Transfer Factors for Agricultural and Animal Products.* doi:10.2172/15010186

Sudret, B. (2008). Global Sensitivity Analysis Using Polynomial Chaos Expansions. *Bayesian Networks in Dependability, 93*(7), 964-979. doi:10.1016/j.ress.2007.04.002

Swiler, L. P., Basurto, E., Brooks, D. M., LaForce, T., Leone, R., Mariner, P. E., . . . Hay, T. (2024). *Uncertainty and Sensitivity Analysis Methods and Applications in the GDSA Framework (FY2024).* Sandia National Laboratories, SAND2024-11075R., Albuquerque NM.

Swiler, L. P., Becker, D.-A., Brooks, D., Govaerts, J., Koskinen, L., Kupiainen, P., . . . Svitelman, V. (2021). *Sensitivity Analysis Comparisons on Geologic Case Studies: An International Collaboration.* Albuquerque, New Mexico: Sandia National Laboratories, SAND2021-11053.

Swiler, L. P., Becker, D.-A., Brooks, D., Koskinen, L., Kupiainen, P., Plischke, E., . . . Spiessl, S. (2025). *Sensitivity Analysis Comparison on Geologic Case Studies: An International Collaboration, Volume 2.* Sandia National Laboratories, SAND2025-00230, Albuquerque, NM.

Swiler, L. P., Brooks, D. M., Portone, T., Basurto, E., Mariner, P. E., & Leone, R. (2023). *Uncertainty and Sensitivity Methods and Applications in the GDSA Framework (FY2023).* Albuquerque, NM: Sandia National Laboratories SAND2023-0855 R. .

Swiler, L., Basurto, E., Brooks, D., Eckert, A., Leone, R., Mariner, P., . . . Smith, M. (2022). *Uncertainty and Sensitivity Analysis Methods and Applications in the GDSA Framework (FY2022).* Albuquerque, New Mexico: Sandia National Laboratories, M3SF-22SN01030408, SAND2022-11220 R.

Swiler, L., Basurto, E., Brooks, D., Eckert, A., Leone, R., Mariner, P., . . . Stein, E. (2021). *Uncertainty and Sensitivity Analysis Methods and Applications in the GDSA Framework (FY2021).* Albuquerque, New Mexico: SAND2021-9903R. Sandia National Laboratories.

Swiler, L., Basurto, E., Brooks, D., Eckert, A., Mariner, P., Portone, T., & Stein, E. (2020). *Advances in Uncertainty Quantification and Sensitivity Analysis Methods and Applications in GDSA Framework.* Albuquerque, New Mexico: SAND2020-10802R. Sandia National Laboratories.

Swiler, L., Helton, J., Basurto, E., Brooks, D., Mariner, P., Moore, L., . . . Stein, E. (2019). *Status Report on Uncertainty Quantification and Sensitivity Analysis Tools in the Geologic Disposal Safety Assessment (GDSA) Framework.* Albuquerque, New Mexico: SAND2019-13835R. Sandia National Laboratories.

U.S. DOE. (2008). *Yucca Mountain Repository License Application Safety Analysis Report. DOE/RW-0573, Revision 1, http://www.nrc.gov/waste/hlw-disposal/yucca-lic-app/yucca-lic-app-safety-report.html#1.* Washington, D.C. : U.S. Department of Energy.

U.S. DOE. (2014). *Title 40 CFR Part 191 Subparts B and C Compliance Recertification Application 2014 for the Waste Isolation Pilot Plant. DOE/WIPP 15-3503.* Carlsbad, New Mexico: U.S. Department of Energy.